Regional-Scale Mineral Exploration Through Joint Inversion and Geology Differentiation Based on Multiphysics Geoscientific Data in the QUEST Project Area

Jae Deok Kim[13], Jiajia Sun[1], Aline Melo[24]

[1]Department of Earth and Atmospheric Sciences, University of Houston, Houston, TX, USA
[2]Departamento de Geologia, Instituto de Geociencias, Universidade Federal de Minas Gerais, Brazil
[3]Presently at MIT-WHOI Joint Program in Oceanography/Applied Ocean Science & Engineering, Cambridge and Woods Hole, MA, USA
[4]Presently at School of Earth Sciences, University College Dublin, Ireland

Key Points:

- Quantitative integration of multiphysics geoscientific data improves interpretation and reduces exploration risk
- Our workflow combines joint inversion and geology differentiation to construct a 3D quasi-geology model that shows the spatial distribution of different geological units
- Applying the workflow to the QUEST project data reveals an area beneath a glacial overburden where more detailed surveys may help assess the mineral prospectivity of the region

Corresponding author: Jiajia Sun, jsun29@central.uh.edu

Abstract

Airborne geophysics is widely used in regional-scale mineral exploration because it provides rapid collection of multiple types of geophysical data over large areas. The availability of multiphysics data is potentially useful because the complementary information contained in the multiple data sets can be integrated into a common earth model consistent with all available data and prior information. However, quantitative integration of regional-scale multiphysics airborne geophysical data is rarely reported in literature. To fully tap into the complementary information contained in airborne gravity and magnetic data for regional-scale mineral exploration, we followed a workflow that focuses on two key components: joint inversion and geology differentiation. Joint inversion allows the models to constrain each other at the inversion stage, resulting in structurally similar physical property models and enhanced correlations between inverted physical property values. Geology differentiation classifies the jointly inverted physical property values into distinct classes and builds a 3D quasi-geology model that shows the spatial distribution of different geological units. Prior geological information from various sources is also used when performing geology differentiation. We first tested this workflow on synthetic data before applying it to a set of airborne gravity and magnetic data from the Quesnel terrane in central British Columbia. We have successfully identified 9 different geological units that are consistent with the airborne geophysical data and prior geological information in the QUEST project area. Our results allowed for a more detailed classification of the geology beneath a thick overburden of glacial sediments and we have also identified potential targets for future detailed surveys that are spatially correlated to known mineral deposits (Mount Milligan, Lorraine, Takla-Rainbow, and Kwanika deposits). Our work provides guidance for follow-up detailed surveys in the Quesnel terrane and highlights the benefits of integrated interpretation of multiphysics geoscientific data.

Plain Language Summary

With global energy transition, the demand for minerals is expected to increase dramatically in the coming decades. Therefore, an urgent need exists of discovering more minerals. However, mineral exploration is increasingly focused on areas with thick sedimentary covers, which makes direct sampling difficult and surface geology work less useful. Geophysics, as a non-invasive method, can provide structural and compositional information in the subsurface. We focused on an under-explored region of British Columbia between Williams Lake and Mackenize. This area is of interest because it hosts several known copper and gold porphyry deposits in the north and south parts, whereas the central part is overlain by a thick overburden of glacial sediments. Our goal is to use the publicly available airborne geophysical data to map out prospective areas for mineral exploration in the central part. We used two techniques to accomplish our goal, namely, geophysical inversion and geology differentiation. The geophysical inversion in the first step allowed us to construct a 3D density contrast model and a 3D magnetic susceptibility model. The distribution of the recovered density and susceptibility values and their spatial variations reflect the subsurface geology. In the second step, we classified the recovered density contrast and susceptibility values into 9 classes, each of which is characterized by unique ranges of physical property values, and represents one distinct geological unit. We found significant correlation between known mineral deposits and Classes 2 & 3 in the north and south parts of our study area. Those geological bodies corresponding to Classes 2 & 3 in the central part were, therefore, identified as prospective targets for detailed follow-up geophysical surveys and study. Our work shows that 3D geophysical inversion, when combined with geology differentiation, can help identify prospective areas for mineral exploration on a regional scale.

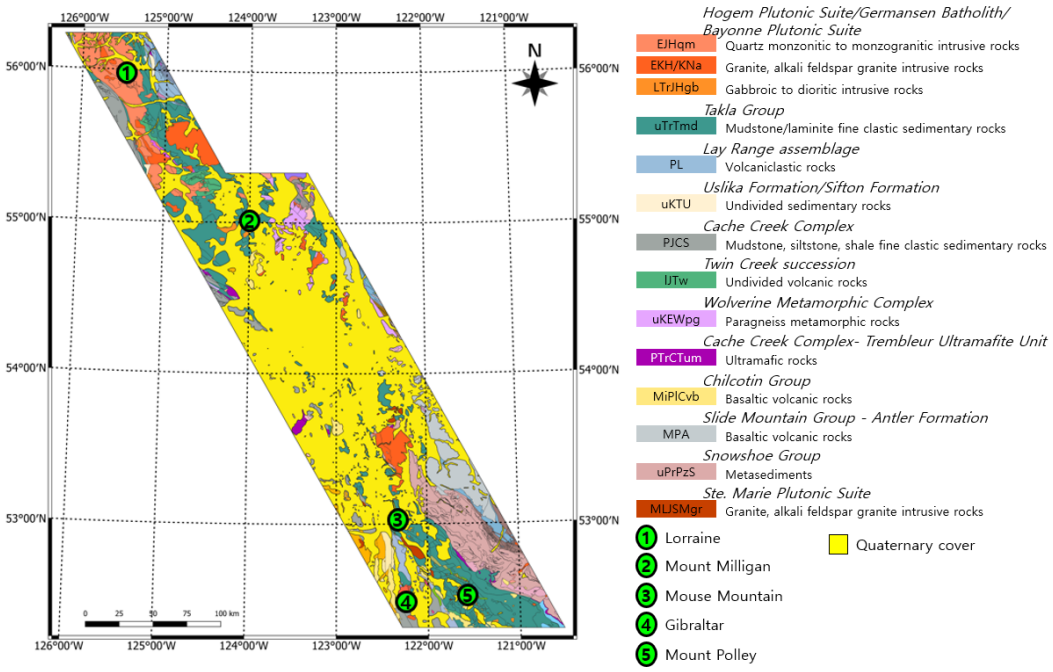

Figure 1. Geological map of the QUEST survey area, after Cui et al. (2017), with the locations of some known mineral deposits shown in green circles: 1) Lorraine, 2) Mount Milligan, 3) Mouse Mountain, 4) Gibraltar, 5) Mount Polley deposits. Shown in yellow is the Quaternary sediment layer that overlays most of the central part of the Quesnel terrane. Note only the most representative units are presented on the legend to the right.

1 Introduction

The QUEST project, standing for Quesnellia Exploration Strategy, was carried out to collect geological, geophysical, and geochemical data in central British Columbia between Williams Lake and Mackenzie with the purpose of stimulating mineral exploration in underexplored regions (Geoscience BC, 2008). Geophysical data, including airborne gravity, magnetic, and electromagnetic (EM) data, were collected throughout the years 2007 and 2008 and were primarily focused on the Quesnel terrane, which is highly prospective for copper and gold porphyry deposits as it is the host of several known mineral ore deposits (e.g. Mount Milligan, Mount Polley, Gibraltar deposits). The northern and southern parts of the survey area have exposed bedrock and outcrops that have helped assess the mineral prospectivity of the region. The central part, however, is largely underexplored due to a thick layer of Quaternary glacial sediments and till. Figure 1 shows a geological map with the glacial overburden in yellow and the locations of some known mineral ore deposits (Cui et al., 2017).

Previous work on the QUEST geophysical data was presented in Phillips et al. (2009) and Kowalczyk et al. (2010), where the airborne gravity, magnetic, and EM data have been inverted separately. They interpret the inverted physical property models through a classification process with the argument that separating the models into groups of cells with similar properties and mapping these in the 3D spatial domain may serve as a proxy for geology. Phillips et al. (2009) classified each point in the density contrast-susceptibility crossplot and incorporated the inverted electrical conductivity values to their classification by color-coding each point in the crossplot by its corresponding conductivity value. The authors divided the inverted density contrast and susceptibility values each into 3

arbitrary classes of high, medium, and low values, resulting in a total of 9 classes. They also extended this classification to include the background conductivity model with high, medium, and low cut-offs, leading to a classification of 27 classes. However, as the authors stated, this classification scheme involves a high degree of subjectivity. Kowalczyk et al. (2010) have classified the inverted density contrast and susceptibility values into 19 classes. Despite the promising results in (Kowalczyk et al., 2010), the geological reasoning behind how each class was defined remains unclear. It is also noteworthy that the identified classes in both Phillips et al. (2009) and Kowalczyk et al. (2010), when visualized in crossplots, are mostly rectangle-shaped, an indication of the arbitrarily determined cut-off values without considering the site specific physical property relationships in the QUEST project area. We argue that a better outcome can be achieved by closely examining the trends, groupings, and relations revealed by geophysical inversions followed by a classification driven by these features instead of some arbitrarily determined cut-off values.

Indeed, the work in both Phillips et al. (2009) and Kowalczyk et al. (2010) show the potential for applying better techniques. Namely, we may improve on the classifications that were based on the recovered physical property models from separate inversions of the geophysical data by implementing joint inversion. Here, we define *separate inversions* as inversions that are performed independently from each other without the exchange of any information between the inversions. We argue that joint inversion could further improve the classification of geological units and potentially lead to new knowledge on the mineral prospectivity of the region for two reasons. First, previous work (e.g., (Fregoso & Gallardo, 2009a; Doetsch et al., 2010a; Infante et al., 2010; Sun et al., 2020)) demonstrates that joint inversion of potential field data leads to better defined linear features with lesser amount of scattering, which allows the subsequent classification to work less subjectively and potentially more reliably because the classification is largely driven by the linear features revealed by joint inversion. Secondly, previous work such as Oldenburg et al. (1997) and Phillips et al. (2001) clearly shows the structural inconsistency or even conflict from separate inversions, which presents challenges during interpretation as many judgment calls must be made to reconcile the inconsistent features based on an interpreter's experience or geological perception. However, when a structure-based joint inversion is implemented, such as cross-gradients joint inversion (Gallardo & Meju, 2003), the structural information in the density contrast model is used to constrain the structures in the susceptibility model, and vice versa. Complementary structural information, if it exists in the QUEST geophysical data and is effectively used during inversion, will result in density contrast and susceptibility models that are more structurally consistent with each other. The enhanced structural similarity will facilitate the classification of inverted physical property values and will be less subjective as the need of reconciling inconsistent features is largely reduced.

The goal of our work is to improve upon the previous work on the QUEST geophysical data and to further our understanding of the mineral prospectivity in the Quesnel terrane, especially under the glacial overburden, through the integrated interpretation of multiple geophysical and geological data. We follow the workflow presented by Y. Li et al. (2019). First, multiple geophysical data sets are inverted to obtain physical property models. For our study, we perform joint inversion based on the cross-gradients method (Gallardo & Meju, 2003). Secondly, the jointly inverted physical property values are examined and classified into different groups in the crossplot based on the linear trends revealed by inversion as well as from available geological information in the QUEST project area. Thirdly, the classified groups are mapped and visualized in the 3D spatial domain, which shows the 3D distribution of the various geological units. The whole process, therefore, consists of three components: joint inversion, classification in a crossplot, and visualization in 3D. Following Y. Li et al. (2019), we will refer to the last two components collectively as *geology differentiation* and the final 3D model as *3D quasi-geology model*. The quasi-geology model can then be used to make inferences about the

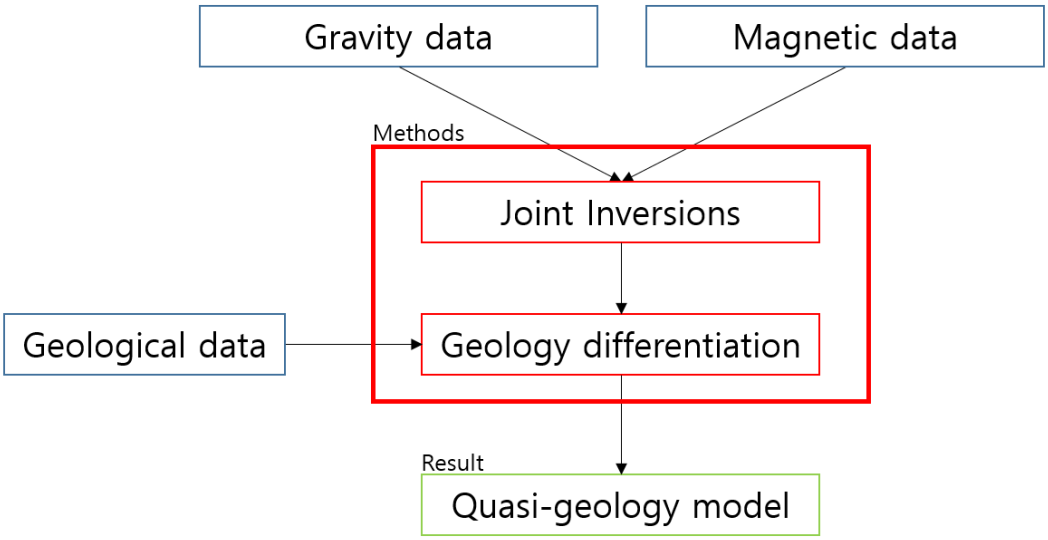

Figure 2. A diagram of the quantitative workflow used in this study for the integrated interpretation of gravity and magnetic data with *a priori* geological information.

geology, and depending on the application, may be used to identify targets for subsequent detailed surveys. A flowchart of the workflow is shown in Figure 2.

We note that our current work is limited to the airborne gravity and magnetic data collected over the QUEST project area due to the following two reasons. First, being able to perform 3D inversions of massive regional-scale EM data alone is at the forefront of EM research. Jointly inverting regional-scale airborne gravity, magnetic, and EM data in a unified 3D framework is yet to be achieved. Indeed, it has not been reported in literature. Secondly, the airborne EM data have a very different depth of investigation (less than 1 km) than the gravity and magnetic data. Whether joint inversion of the three data sets would result in better geophysical models remains unknown and requires more work. We, therefore, defer the incorporation of the airborne EM data to future work.

For the following sections of this manuscript, we begin with the description of the workflow used for this study where we provide a brief review of joint inversion and geology differentiation. We then illustrate this workflow by applying it to synthetic gravity and magnetic data. Next, we provide a description of the geological setting of the QUEST survey area, followed by the presentation of the collected airborne gravity and magnetic data with a brief overview of the processing steps that the data has undergone. We have included a section to describe the procedures used to estimate the data errors, a step that has proven critical in the inversions of field data. Lastly, we present the application of the workflow to the QUEST data. We first jointly inverted the airborne gravity and magnetic data to obtain 3D density contrast and susceptibility models. We then performed geology differentiation based on the jointly inverted physical property values and available geological data. The final product of this study comes in the form of a 3D quasi-geology model with identified targets for future detailed surveys that may help investigate the prospectivity of mineral deposits in the underexplored regions.

2 Methods

The two main components of the quantitative workflow for the integrated interpretation of multiple geophysical and geological data used for this study are joint inver-

sion and geology differentiation (Figure 2). As defined in Moorkamp et al. (2016), *joint inversion* refers to a unified numerical framework where different data sets are inverted simultaneously within the same optimization process. An essential component of joint inversion is a strategy determining how the exchange of information between different models is realized. This strategy is typically summarized by a coupling term. Depending on the specific form of the coupling term, joint inversion can enhance either structural similarity (Gallardo & Meju, 2003; Linde et al., 2006) or physical property correlations (Afnimar et al., 2002; Lelièvre et al., 2012; Kamm et al., 2015) between the inverted physical property models. A favorable consequence of the enhanced structural similarity and physical property correlations is that the subsequent geology differentiation can be done less subjectively and potentially more reliably, as shown by recent works (Y. Li et al., 2019; Astic et al., 2020; Sun et al., 2020). Below, we describe the joint inversion and geology differentiation methodologies used for this study.

2.1 Joint Inversion

In this study, we employ the smoothness-based Tikhonov regularization methods as described in Y. Li and Oldenburg (1996, 1998a) to invert the gravity and magnetic data. The goal of the regularized inversion is to find the smoothest model that can fit the data within a desired error tolerance. Mathematically, the inverse problem can be solved as an optimization problem that seeks to minimize the following objective function:

$$\phi(\mathbf{m}) = \left\|\mathbf{W}_d\left(\mathbf{d^{obs}} - \mathbf{F}[\mathbf{m}]\right)\right\|_2^2 + \beta\left\|\mathbf{W}_m\left(\mathbf{m} - \mathbf{m^{ref}}\right)\right\|_2^2 \tag{1}$$

where the first term is the data misfit term that measures the difference between the observed and predicted data, and the second term is the model regularization term which measures the complexity of the model. Here, $\mathbf{m}$ is the model vector, $\mathbf{d^{obs}}$ is the observed data, $\mathbf{F}$ is the forward modeling operator, $\mathbf{W}_d$ is the data weighting matrix that incorporates the data uncertainties and their correlations, $\mathbf{W}_m$ is the model weighting matrix that incorporates the smallness and smoothness of the model, and $\mathbf{m^{ref}}$ is a reference model that reflects any *a priori* information about the geology or physical property model (Oldenburg & Li, 2005). We also incorporate the sensitivity-based spatial weighting as described in Y. Li and Oldenburg (2000) into $\mathbf{W}_m$ to counteract the decay of the gravitational or magnetic effect with distance (Y. Li & Oldenburg, 1996, 1998a). Lastly, the regularization or trade-off parameter, β, controls how much each term contributes to the objective function. The value for the regularization parameter is determined based on the target data misfit value.

For joint inversion, the objective function to be minimized is an extension of equation (1). For the case of joint inversion of two different data sets, the objective function is

$$\begin{aligned}\phi(\mathbf{m_1}, \mathbf{m_2}) = &\left\|\mathbf{W}_{d1}\left(\mathbf{d_1^{obs}} - \mathbf{F_1}(\mathbf{m_1})\right)\right\|_2^2 + \beta_1\left\|\mathbf{W}_{m1}\left(\mathbf{m_1} - \mathbf{m_1^{ref}}\right)\right\|_2^2 + \\ &\left\|\mathbf{W}_{d2}\left(\mathbf{d_2^{obs}} - \mathbf{F_2}(\mathbf{m_2})\right)\right\|_2^2 + \beta_2\left\|\mathbf{W}_{m2}\left(\mathbf{m_2} - \mathbf{m_2^{ref}}\right)\right\|_2^2 + \\ &\lambda\sum_{i=1}^{M}\left[\left\|\nabla\mathbf{m_1}^{(i)}\right\|_2^2\left\|\nabla\mathbf{m_2}^{(i)}\right\|_2^2 - \left(\mathbf{m_1}^{(i)}\cdot\mathbf{m_2}^{(i)}\right)^2\right]\end{aligned} \tag{2}$$

where $\mathbf{m_{1,2}}$ are two different physical property models and the last term is the coupling function which defines how the two different physical properties are coupled. Here, λ is the weighting parameter for the coupling function. For our coupling function, we used cross-gradients, but instead of using the cross-product form defined by Gallardo and Meju (2003), we used the equivalent dot-product form because the latter is easier to handle numerically, especially when deriving its gradient. Our joint inversion code was developed as part of an open-source Python framework for geophysical inversions, Simulation and Parameter Estimation in Geophysics (SimPEG - https://simpeg.xyz/) (Cockett et al., 2015).

2.2 Geology Differentiation

Geology differentiation is the process of identifying different geological units using multiple physical property models that are recovered from geophysical inversions (Y. Li et al., 2019). Some applications of geology differentiation include alteration zones mapping (Hanneson, 2003; N. C. Williams et al., 2004; N. Williams & Dipple, 2007; Goodwin & Skirrow, 2019) and lithology mapping (Fraser et al., 2012; Martinez & Li, 2015; A. Melo & Li, 2016; A. T. Melo et al., 2017; A. T. Melo & Li, 2019; Astic et al., 2020; Sun et al., 2020; K. Li et al., 2021; Wei & Sun, 2021). Geology differentiation is typically performed by first visualizing the recovered physical property values in a crossplot which are then classified into distinct classes. Each class is characterized by a unique range of physical property values. A critical task when performing geology differentiation is to determine how to classify the inverted values into different classes. When prior geological information is sparse and when physical property measurements are not available, the classification can be done by inspecting the natural trends (such as linear trends) and groupings that occur among the inverted values in the crossplot. Previous work (Sun et al., 2020; K. Li et al., 2021) shows that valuable information about subsurface geological structures and compositions can be extracted using such approach. On the other hand, if prior physical property measurements on rock samples in a study area are available, the expected ranges of physical property values for different geological units can be established, based upon which classification of the inverted values can be achieved. Previous work, such as A. T. Melo et al. (2017), demonstrates the effectiveness of this approach. The identified geological units can then be mapped onto the 3D spatial domain to construct a 3D quasi-geology model that shows the spatial distributions of the different geological units.

2.3 Summary of the Workflow

Our workflow is summarized in Figure 2. The workflow starts with the availability of multiple geophysical and geological data sets. The multiple geophysical data are then jointly inverted to produce corresponding physical property models. In our case, the availability of gravity and magnetic data allowed us to perform joint inversion to reconstruct density contrast and susceptibility models. Next, based on the linear trends apparent on the crossplot of jointly inverted physical property values, we did an initial classification and visualized the differentiated units in 3D to see if there is any correlation with either the well-defined inverted features (such as large-amplitude density contrast or susceptibility anomalies) or known geological features, such as mineral deposits. In an iterative manner, the bounds between the different classes were adjusted until we achieved a reasonable correlation with the main geophysical or geological features. The identified classes were then visualized into a 3D quasi-geology model to provide insights into the spatial distribution of the different geological units. Depending on the purpose of the study, the 3D quasi-geology model can be used to make inferences about the underlying geology, or if needed, to define new targets for subsequent detailed surveys.

Having established the workflow, we proceeded by first testing its validity on synthetic gravity and magnetic data. A synthetic test allows us to test the workflow in a controlled setting to verify both the validity and the effectiveness of the workflow. It also provides us with evidence that our assumptions are valid and gives us an opportunity to manage or control parameters that may affect the results before applying it to the field data. Thus, when properly conducted, a synthetic test provides us with a proof of concept for the workflow.

3 Synthetic Test

We present a synthetic example to better illustrate the workflow for the integrated interpretation of multiple geophysical and geological data based on joint inversion and

Table 1. Physical property values of the causative bodies for the synthetic test

Unit	Density contrast ($g\,cm^{-3}$)	Magnetic susceptibility (SI)
A	-0.3	0.03
B	-0.3	0.1
C	0.3	0.1
D	0.3	0.03

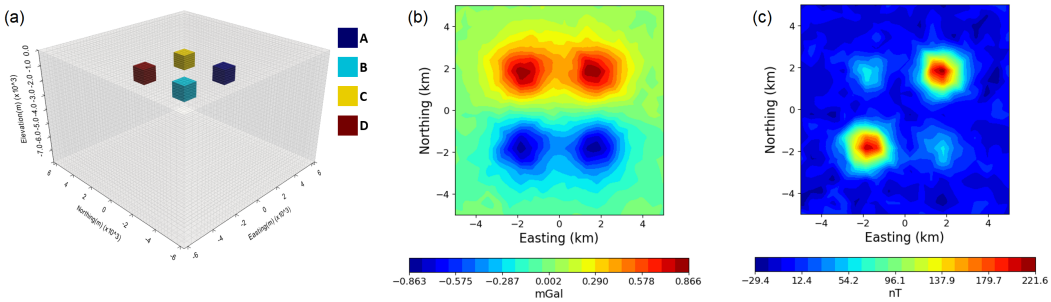

Figure 3. (a) 3D view of the true causative bodies, (b) simulated gravity data and (c) simulated TMI data.

geology differentiation. The example consists of gravity and purely induced total magnetic intensity (TMI) data simulated from four causative bodies. The causative bodies are cubes with lengths 1 km on all sides and depth to the top of the blocks is 1 km. The models exist in a mesh consisting of 40 cells in both the easting and northing directions, and 25 cells in depth. Each cell is a cube with length 250 m on each side. Padding cells of increasing dimensions are also added in all directions. The four causative bodies are located at the center region of the mesh with background values of 0. The physical property values for each causative body are summarized in Table 1.

3.1 Synthetic Data

Data is simulated on the surface with 400 observations placed on a regular grid of size 10 km × 10 km and observation points are placed 1 m above the ground. Uncorrelated Gaussian noise with standard deviation of 0.035 mGal is added to the gravity data, while uncorrelated Gaussian noise with standard deviation of 10 nT is added to the TMI data. For the TMI data, we assumed an inclination of 90°, declination of 0°, and inducing field strength of 50,000 nT. The simulated gravity data shows positive anomalies where density contrast is positive and negative anomalies where density contrast is negative. Likewise, the simulated TMI data shows high magnetic anomalies where susceptibility is high and low magnetic anomalies where susceptibility is low (Figure 3).

3.2 Joint Inversion

We first performed separate inversions of the synthetic gravity and TMI data to establish a comparison with joint inversion. For brevity, the results from separate inversions are not shown as the focus of the workflow is on joint inversion. However, it is worth noting that performing separate inversions before performing joint inversion may be beneficial, especially in determining some of the parameters in the joint inversion, such as the weight of the coupling function and the regularization parameters. Sections from the

jointly inverted density contrast model are shown in Figure 4 and sections from the jointly inverted susceptibility model are shown in Figure 5. We observe that the anomalous bodies are recovered at roughly the right locations and depths. The jointly inverted models are able to reproduce the data, although the residuals show some correlated features around the anomalies (Figure 6). This shows that the joint inversion is able to generally fit the data, but missed some information around the anomalies. This may be remedied by using a smaller target data misfit (but at the risk of fitting noise) or using an adaptive method where the data uncertainties around the anomalies are reduced so as to fit them better.

3.3 Geology Differentiation

As the first step to geology differentiation, we visualized the inverted physical property values in a crossplot, where each point represents one model cell. For comparison, we have included the crossplot from separate inversions as well (Figure 7). Both crossplots summarize the variations of the inverted physical property values and present natural trends on how the values are distributed. Although the crossplots exhibit a first-order similarity on the range of values, it is clear that the jointly inverted values present four well-defined linear features. The same kind of linear features have been discussed previously by other researchers (Linde et al., 2006, 2008; Fregoso & Gallardo, 2009b; Doetsch et al., 2010b; K. Li et al., 2021; Sun et al., 2020).

The next step is to classify the inverted values into different classes depending on what is expected from different geological units. In this case, we can easily identify four distinct units from the crossplot of jointly inverted values based on the linear trends, as shown in Figure 8. The points that were not classified to any of the causative bodies are considered background, and thus were not shown in the visualizations. The boundaries between the background and the four units were determined experimentally through trial and error. The guiding principle is that the background unit, when visualized in 3D, should not contain any significant density contrast or susceptibility anomalies. We show a 3D view of the true causative bodies in Figure 3(a) and the units we identified through the process of geology differentiation in Figure 9. As shown, the four causative bodies are identified at roughly the right locations. However, the bodies are round, smooth, and seem to extend to the surface, whereas the true bodies do not. This is a result of the smoothness regularization applied to the inversions, which will cause the neighboring values to vary smoothly. As a result of such smoothness, the causative bodies look like they extend smoothly towards the surface.

There are several ways to deal with the limitations from the smoothness regularization. First, when classifying the units, we can intentionally limit each unit to the larger values. This helps shrink the volume of the differentiated units. For example, we may shrink the bounds of each unit (A, B, C and D) identified in Figure 8 so that each unit contains less of the points close to the background unit. Figure S1 in the supporting information shows an example of such reduced classification and Figure S2 shows the geological units resulting from this reduced classification. Secondly, a sparse norm regularization can be used to recover compact bodies. We point out that the second strategy is at the forefront of research (X. Li & Sun, 2021). Also, the computational time will increase rapidly with sparse norms. As the first attempt to jointly invert the potential field data sets in the QUEST area, we chose to use the smoothness regularization as implemented in SimPEG (Cockett et al., 2015) despite the limitations mentioned above.

3.4 Discussion

The results above show that cross-gradient joint inversion is able to better define the boundaries between anomalous bodies by enhancing structural similarity between the physical property models. The distribution of inverted physical property values was

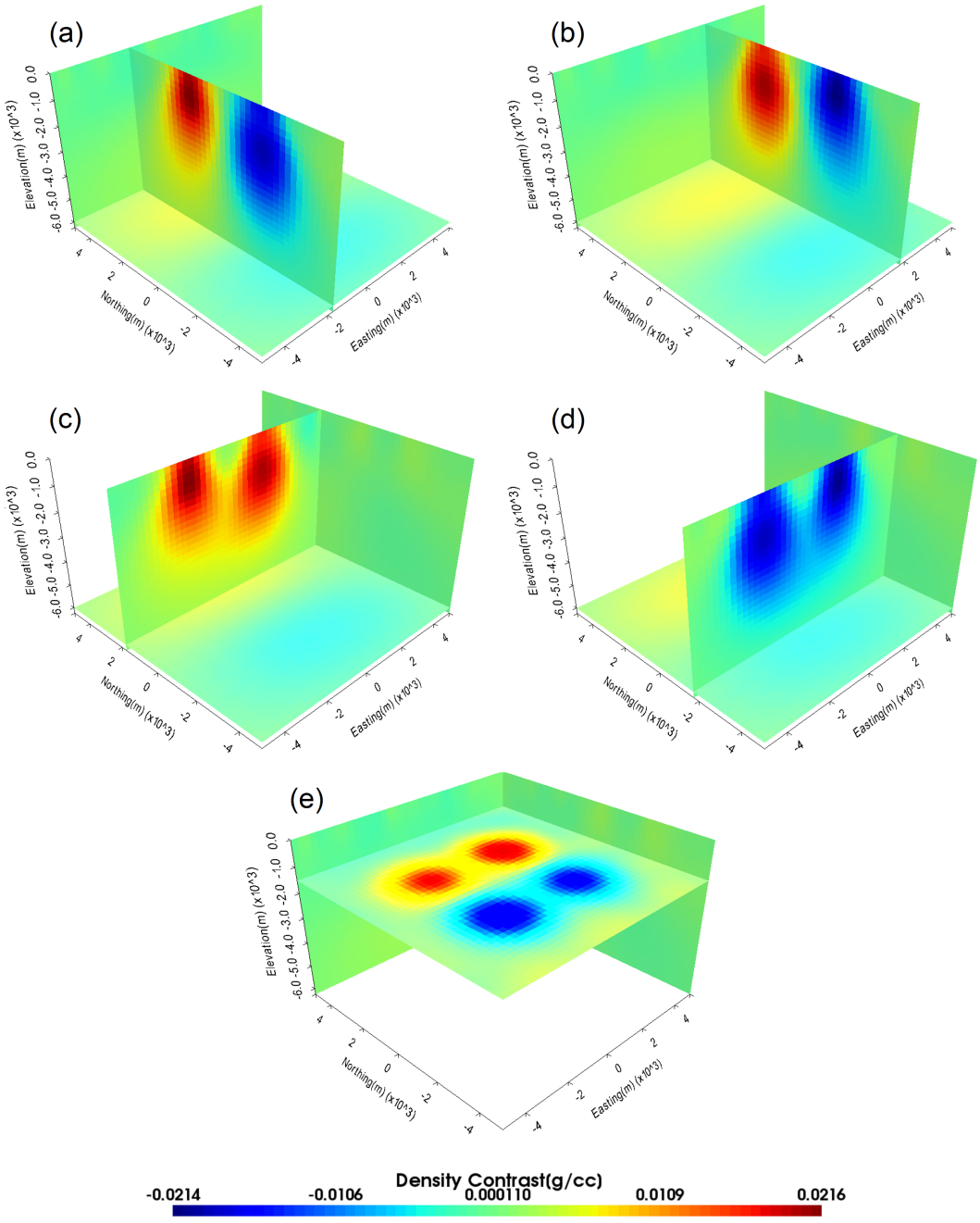

Figure 4. Density contrast model recovered from joint inversion with vertical sections on (a) easting=−1750 m, (b) easting=1750 m, (c) northing=1750 m, (d) northing=−1750 m, and (e) a horizontal section on elevation=−1500 m.

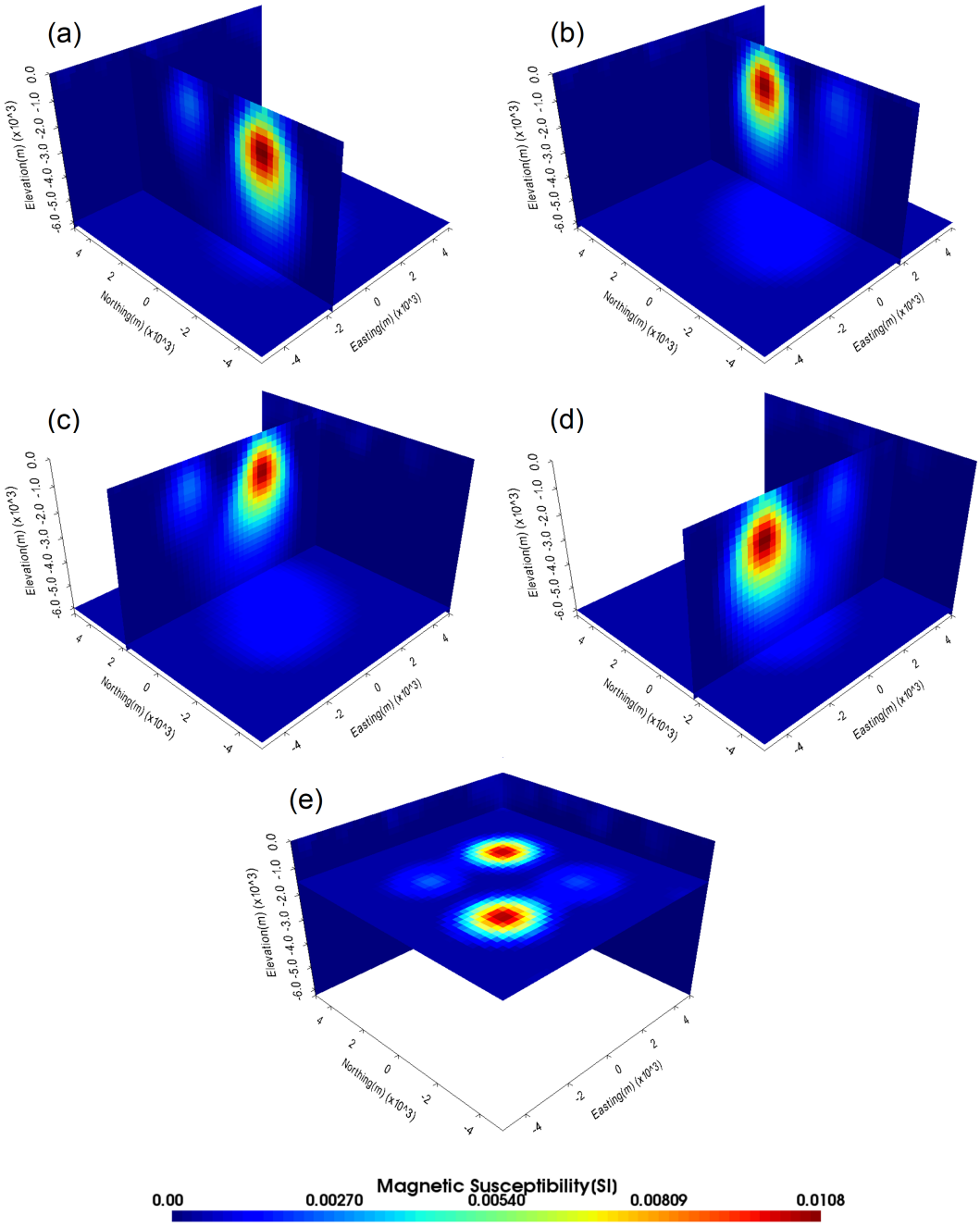

Figure 5. Susceptibility model recovered from joint inversion with vertical sections on (a) easting=−1750 m, (b) easting=1750 m, (c) northing=1750 m, (d) northing=−1750 m, and (e) a horizontal section on elevation=−1500 m.

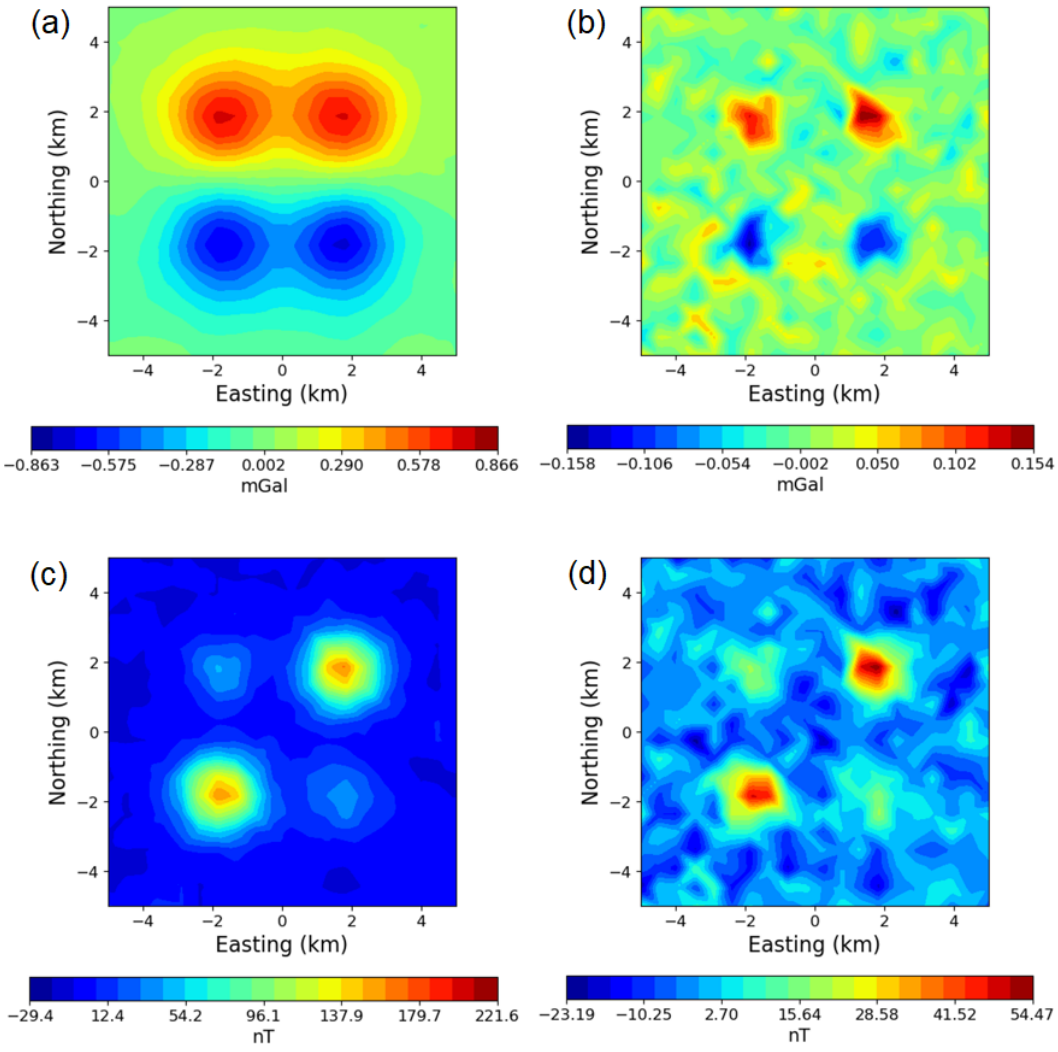

Figure 6. (a) Predicted gravity data and (b) gravity data residual from the jointly inverted density contrast model. (c) Predicted TMI data and (d) TMI data residual from the jointly inverted susceptibility model.

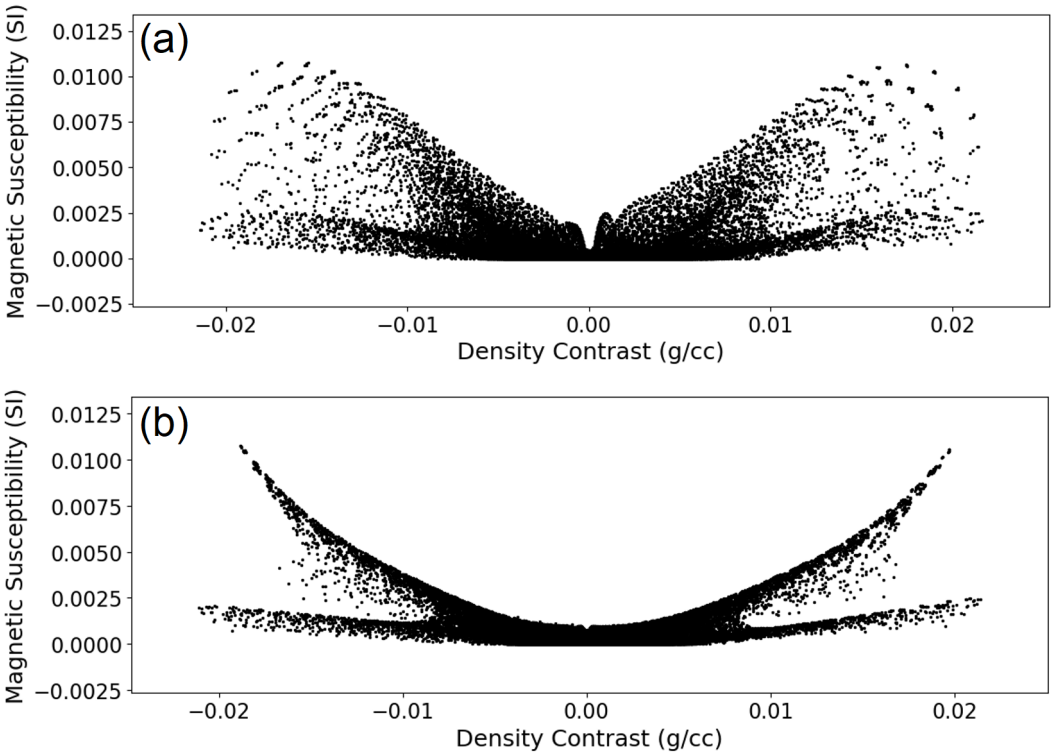

Figure 7. (a) Crossplot of separately inverted susceptibility and density contrast values. (b) Crossplot of jointly inverted susceptibility and density contrast values. Each point in the plots represents one model cell.

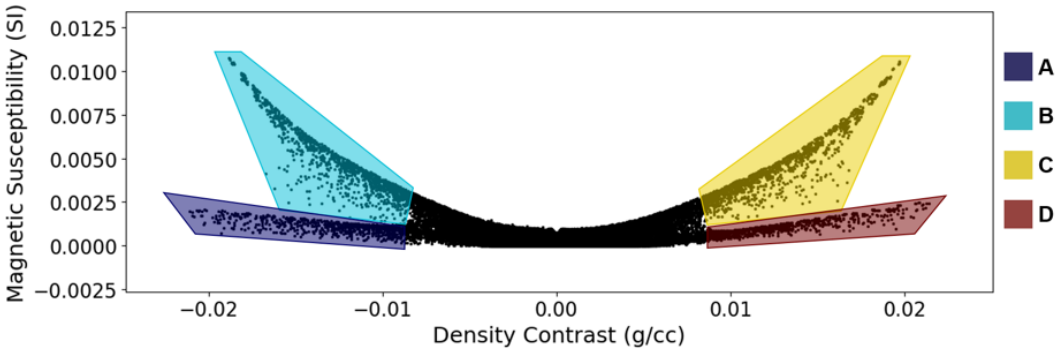

Figure 8. Classification applied on the crossplot of jointly inverted susceptibility and density contrast values where each color-coded polygon represents a different causative body.

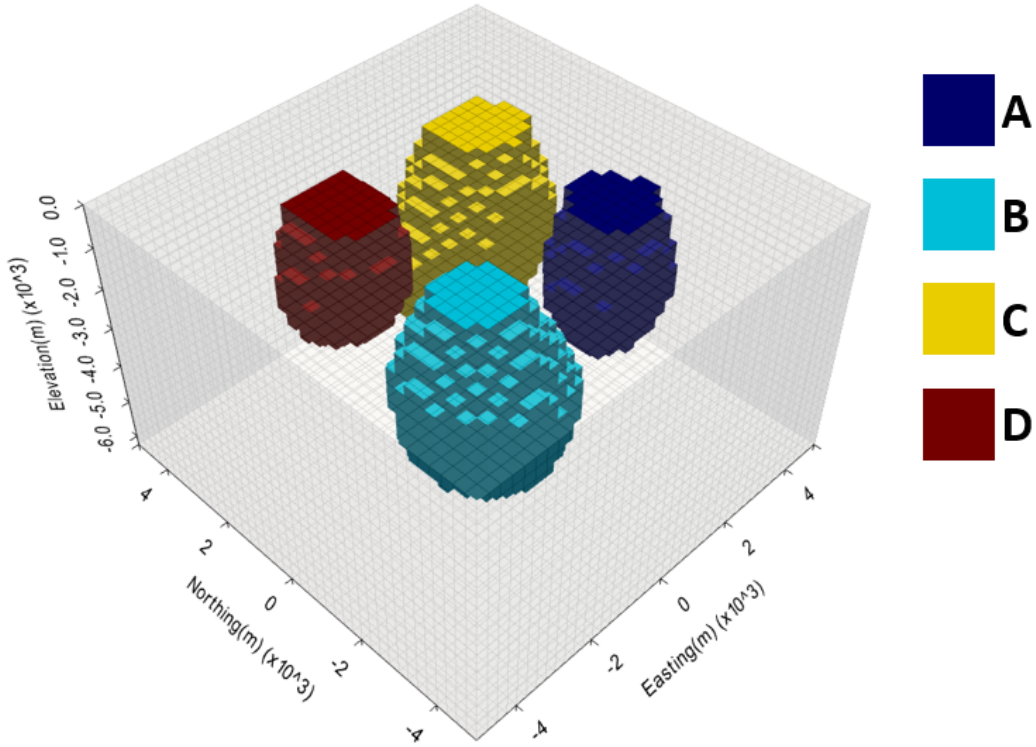

Figure 9. 3D view of the causative bodies identified through geology differentiation based on the jointly inverted values.

better constrained for joint inversion than for separate inversions; separately inverted physical property values presented severe scattering in the crossplot of inverted values. Geology differentiation based on the jointly inverted values proved effective as it was easier to identify different geological units. Despite the shortcomings from the smoothness regularization, the workflow proved effective as the causative bodies were identified at roughly the correct locations and depths. Thus, the synthetic experiment showed promise for the application of the workflow on field data.

4 Application to the QUEST Data

4.1 Geological Setting

The study area focuses on the Quesnel terrane located in British Columbia, Canada. The Quesnel terrane is an early Mesozoic volcanic arc and contains significant Cu-Mo and Cu-Au porphyry deposits (Schiarizza, 2003; Logan & Mihalynuk, 2014). The Quesnel terrane is considered to contain significant potential for alkalic and calc-alkalic porphyry-type deposits as evidenced by mineral deposits in the region (e.g. Highland Valley, Lornex, Lorraine, Mount Milligan, Mount Polley deposits, among others). Mineralization in the more prolific porphyry deposits in the region are associated to a magmatic arc complex that formed during a 15 million year epoch between the Triassic and Jurassic, where peak mineralization was reached within a 6 million year window centered at 205 Ma (Logan & Mihalynuk, 2014). The late Triassic-early Jurassic intrusive rocks of the Quesnel terrane, including calc-alkaline and alkaline intrusions as well as other mafic and ultramafic intrusions, are of special economic value as it is these that make the Quesnel terrane an important metallogenic province. Additional details on the geological history and bedrock

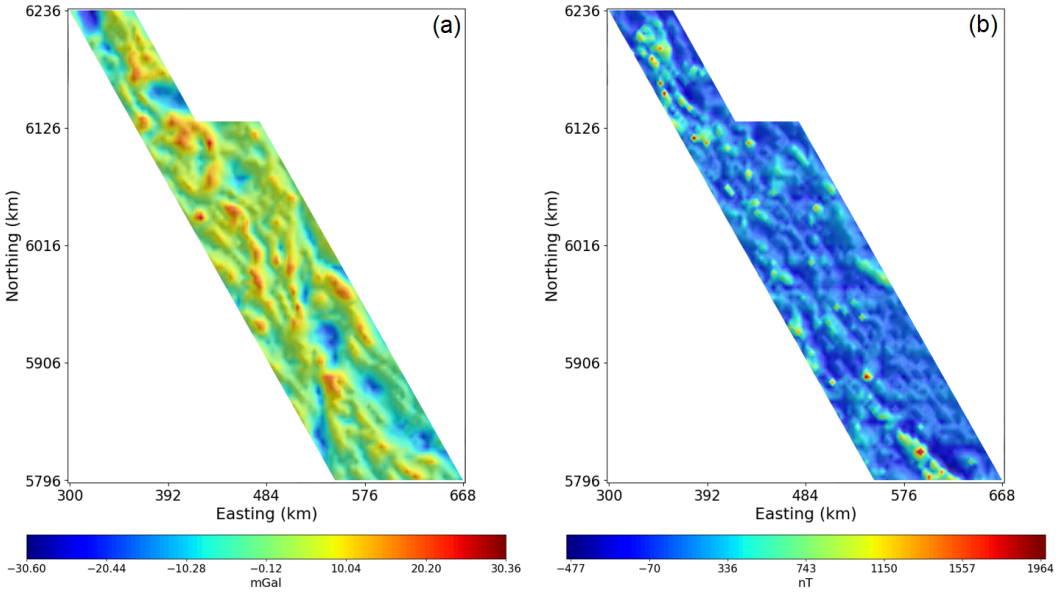

Figure 10. (a) The airborne gravity data after regional field removal and (b) the airborne TMI data after regional field removal. For better visualization of the TMI data, we set the maximum and minimum of the colorbar to the 99.9^{th} and 0.1^{th} percentiles, respectively.

geology of the Quesnel terrane are presented by Schiarizza (2003) and Logan and Mihalynuk (2014).

Most of the central portion of the Quesnel terrane is covered by a ubiquitous Quaternary glacial sediment overburden that has impeded exploration efforts (Figure 1). Geophysical methods are particularly useful in imaging subsurface rocks and structure through such thick sediment layers, because geophysical data, collected on or above the surface, contains valuable information about the subsurface structure as long as the subsurface geological units or structures show spatial variations in their physical properties. Thus, the QUEST data, shown in Figure 10, holds great importance in mapping out the underlying structure and geology of the Quesnel terrane, especially in the central portion overlain by the glacial sediment overburden.

There have been many geological studies done on this region of British Columbia resulting in numerous geological maps. The British Columbia Geological Survey (BCGS) maintains a repository of all these geological maps as the "British Columbia digital geology" (Cui et al., 2017). Numerous geological units were identified using BCGS's Digital Geology database (Cui et al., 2017). However, the geophysical data used in this study is in a regional scale and is not sensitive to all the different geological units. Therefore, we grouped the units into more general groups based on the similarity in rock type and rock composition. The identified geological units are summarized as follows:

1. Ultramafic rocks: serpentinites and other magnesium-rich ultramafic rocks associated with the Cache Creek Complex, the Trembleur ultramafics, the Mason Lakes ultramafics, the Valleau Creek Plutonic Suite, and the Polaris Plutonic Suite.
2. Mafic rocks: basalts, gabbro, dioritic to gabbroic intrusive rocks, gabbro pegmatites, basaltic tuff and breccia associated with the Lounge Lizard Intrusive Suite, Cache Creek Complex, Hogem Plutonic Suite, Witch Lake Formation, Antler Formation, Pillow Ridge Succession, and basalts of the Nicola and Takla groups.

3. Sedimentary and metasedimentary, felsic to intermediate rocks: syenitic to monzonitic intrusive rocks, dioritic intrusive rocks, monzodiorites associated with the Wolverine Range Plutonic Suite, Granite Mountain Batholith, Hogem Batholith, Duckling Creek Syenite Complex, Mount Polley Intrusive Complex, the Endako Group, Kamloops Group, and Lay Range Assemblage. Volcaniclastic and pyroclastic volcanic rocks, phyric andesite, latite and dacite flows associated with the Twin Creek succession and Chuchi Lake succession. Rhyolites and other felsic volcanic rocks, tuffs and breccias associated with the Ootsa Lake group.
4. Metamafic rocks: amphibolite, granodioritic orthogneiss, blueschist, and metabasalts associated with the Cache Creek Complex, Vanderhoof Metamorphic Complex, Wolverine Metamorphic Complex, and the Downey Succession of the Snowshoe Group.
5. Metafelsic rocks: granitic intrusive rocks, granite augen orthogneiss, monzogranites, granodiorites of the Quesnel Lake Gneiss.

The prior geological information presented here was later used to guide the process of geology differentiation. Namely, this information was used in classifying and characterizing the jointly inverted physical property values into various classes. As the information summarized here is a simplification of all the geological units present in the study area, the classification required some adjustments from what was originally expected, and this represents adjustments to the expected values for the physical properties of different geological units after adding information from the inversions. Before we proceed with the results, we first provide an overview of the geophysical data used for this study along with the survey parameters and processing steps that the data has undergone.

4.2 Geophysical Data

The survey area for the QUEST project consists of two parallelograms that run parallel to the Quesnel terrane. The main survey is approximately 386 km in length and 120 km in width; the smaller survey in the North is approximately 120 km in length and 60 km in width. In total, the QUEST project covers an area that exceeds $46,500\,\mathrm{km}^2$. An airborne survey conducted from July to November 2007 collected magnetic (TMI) and time domain electromagnetic (VTEM) data. Another airborne survey conducted from December 2007 to March 2008 collected gravity data. The topography presented challenging terrain as the survey area ranged from rolling hills to steep mountains. The elevation ranged from 380 m to 2,500 m above sea level, with a mean elevation of about 1,000 m.

The airborne gravity survey consisted of traverse lines in the west-east direction with 2,000 m line spacing. Additional control lines were flown at a northwest-southeast direction spaced at 20,000 m and infill lines were flown between the traverse lines in the west-east direction to achieve a spacing of 1,000 m in some locations. The aircraft maintained a nominal terrain clearance of 200 m above ground using a smooth drape surface. The data were collected using airborne gravimeters consisting of three orthogonal accelerometers which remain fixed in inertial space, allowing for corrections of aircraft movement. Precise altitude and location (GPS) measurements were also made onboard the aircraft. Terrain correction was applied at a nominal density of $2.67\,\mathrm{g\,cm}^{-3}$. More details on the gravity survey can be found in Farr et al. (2008).

The airborne TMI data were collected in conjunction to a helicopter-borne versatile time domain electromagnetic (VTEM) survey, which consisted of traverse lines in the west-east direction with 4,000 m spacing between the lines. No tie lines were flown for this survey. The aircraft maintained a nominal terrain clearance of 75 m above the ground. The data were collected using a cesium vapor magnetometer towed 15 m below the aircraft. Precise altitude and location (GPS) measurements were also made onboard the aircraft. A magnetometer and GPS base station were employed to allow for data corrections. The data underwent corrections for diurnal variations based on the recordings

of the base station magnetometer. Some of the data in the northern section of the survey were omitted due to various circumstances that made flying the survey difficult. More details on the magnetic survey can be found in Geotech Ltd (2008).

The Mira Geoscience Advanced Geophysical Interpretation Centre has completed inversions of the QUEST geophysical data sets (Phillips et al., 2009; Kowalczyk et al., 2010). In the process, they have produced residual gravity and TMI data sets where the regional fields have been removed. The removal of regional fields is important to isolate the response from features of interest. The method described in Y. Li and Oldenburg (1998b) was used to separate the regional and residual fields. In this method, a regional inversion is first carried out with a coarse gride size to obtain regional physical property distributions. The regional physical property model is then used to forward model the regional response, after which the regional response is subtracted from the original data to obtain the residual data. Additional details on how the data was processed can be found in Phillips et al. (2009).

For this study, we used the residual data after regional field removal as processed by the Mira Geoscience Advanced Geophysical Interpretation Centre (Phillips et al., 2009) for our own inversions. The gravity and TMI data used for our inversions are presented in Figure 10. Note that for better visualization of the TMI data, we have set the maximum and minimum of the colorbar to the 99.9^{th} and 0.1^{th} percentile, respectively. This was done because the maximum and minimum TMI data values were limited to a few locations which would not have been clearly visible otherwise. For the magnetic inversions, Phillips et al. (2009) have assumed that the inducing field does not vary significantly through the survey area, so parameters corresponding to the center of the survey area and a date halfway through the acquisition (September 15, 2007) were applied. This corresponds to an inducing field strength of $57,254\,\text{nT}$ with an inclination of $74.51°$ and a declination of $20.46°$. We used the same parameters for our magnetic inversions.

The QUEST survey area spans hundreds of kilometers and covers an area of more than $46,500\,\text{km}^2$. The gravity and magnetic data sets each consist of about 400,000 data points and the discretization for the whole survey area using a cell size of 500 m resulted in more than 3 million cells just for the core mesh. Directly inverting the whole data set would be computationally prohibitive. To make the inversion more manageable given the computational resources available to us, we adopted a simple strategy: we split the QUEST survey area into a number of smaller subsets, or 'tiles'. Inversions were then performed on each tile independently from the other tiles and inverted models were finally merged into a single model for the whole survey area. We split the data into 20 tiles as shown in Figure 11. Each tile overlapped with the adjacent tiles so as to ensure good lateral continuity and a smooth merging process for the inverted models, which we explain in a later section and in the supporting information (Text S1).

Before proceeding with the inversion, however, there is a need to determine the noise levels of the observed data as it is required to determine an appropriate target data misfit for the inversions.

4.3 Data Uncertainty Estimation

Estimating the noise levels of geophysical data is important in setting an appropriate target data misfit. Overfitting the data risks fitting the noise, while underfitting the data risks missing important features. As such, it is imperative to understand the data noise levels before proceeding with inversions. We have taken two heuristic approaches to estimating the noise levels of the data and we illustrate their applications to the data in one of the tiles. The gravity data is shown in Figure 12(a) and TMI data is shown in Figure 12(c).

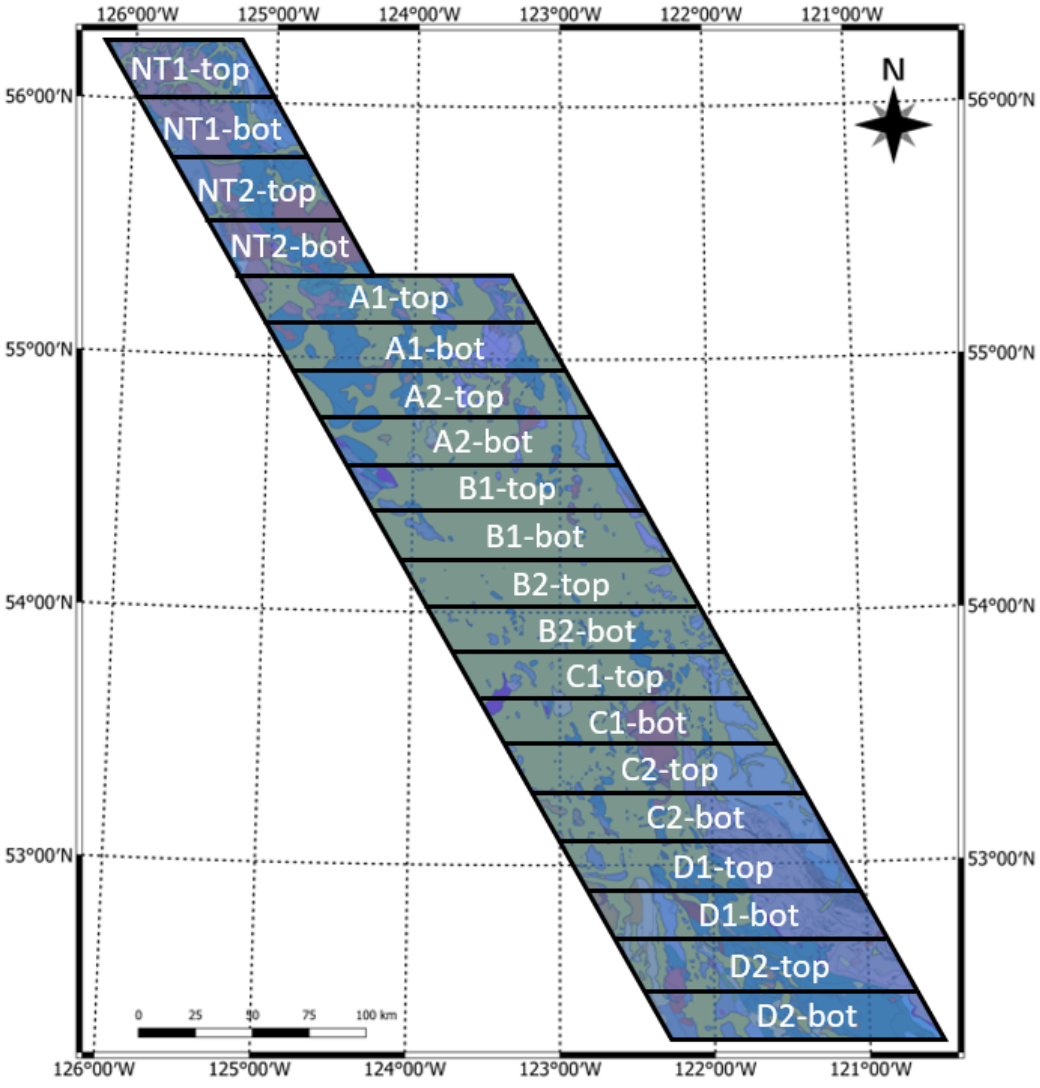

Figure 11. Map showing how the QUEST data were split into different tiles.

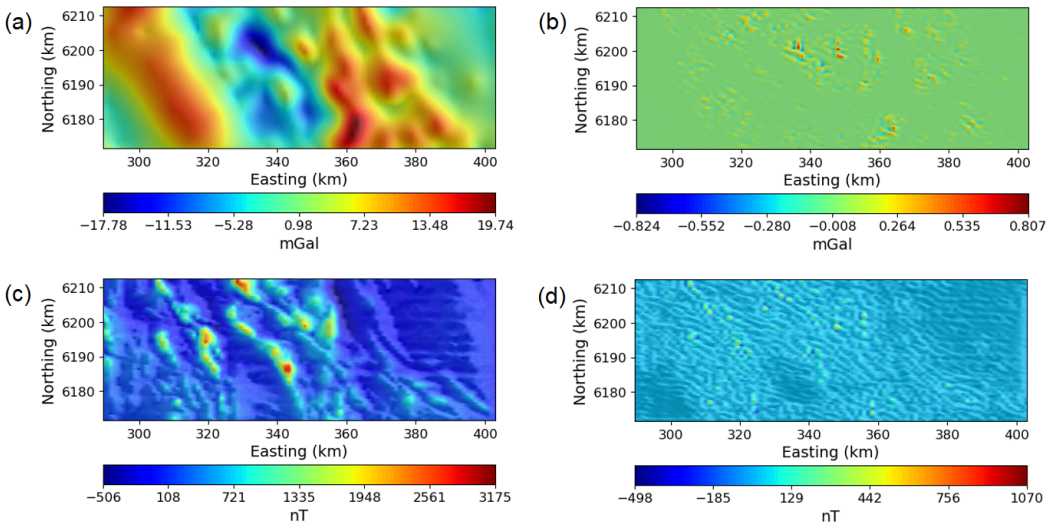

Figure 12. (a) The observed gravity data in the NT1-bot tile and (b) gravity data residual computed from the density contrast equivalent source layer that corresponds to a data misfit of 50. (c) The observed TMI data in the NT1-bot tile and (d) TMI data residual computed from the susceptibility equivalent source layer that corresponds to a data misfit of 2000.

For the first approach, we followed the work from Hansen and O'Leary (1993), to use the L-curve method as an estimator for the error. We first assigned a constant standard deviation of 1 mGal to the gravity data and 100 nT to the TMI data. If the noise is truly random and uncorrelated and if these two noise estimates are indeed true, then the target data misfits for the inversions of both data sets should be equal to the number of data. However, it is unlikely that the initial guesses are anywhere close to the true noise levels. Thus, there is the obvious need of estimating an appropriate target data misfit at these estimated noise levels. We proceeded by constructing a Tikhonov curve through a series of equivalent source layers that fit the data to different degrees; this was achieved by varying the regularization parameters in such a way that the resulting data misfits span several orders of magnitude. The equivalent source layer method is based on the inherent ambiguity of potential fields, where any potential field response can be explained by an arbitrary distribution of sources (Dampney, 1969). It was used here simply to speed up the computations as the technique requires only a single layer to be able to reproduce the data. For each equivalent source layer, the data misfit and regularization values were computed to finally construct Tikhonov curves for each data set (Figure 13).

As can be seen, the Tikhonov curve from the gravity inversions shows a clear "elbow", and following Hansen and O'Leary (1993), the point at the elbow represents the best estimate for the target data misfit given the current noise level estimates. In the case for the gravity data, at a standard deviation of 1 mGal, the target data misfit was estimated to be close to 50. Given that the number of data for this tile was 18,924 measurements, this shows that a standard deviation of 1 mGal for the gravity data is actually an overestimate of the noise level. The standard deviation for the gravity data in this tile should be closer to 0.0514 mGal. We show the residual data computed from the equivalent source layer that resulted in a data misfit of 50 in Figure 12(b). The residual shows mostly random and uncorrelated features, signifying that at this data misfit, the inversion adequately fits the data.

The Tikhonov curve from the magnetic inversions does not show a clear elbow as opposed to the gravity inversions; it is concave and thus it becomes hard to determine

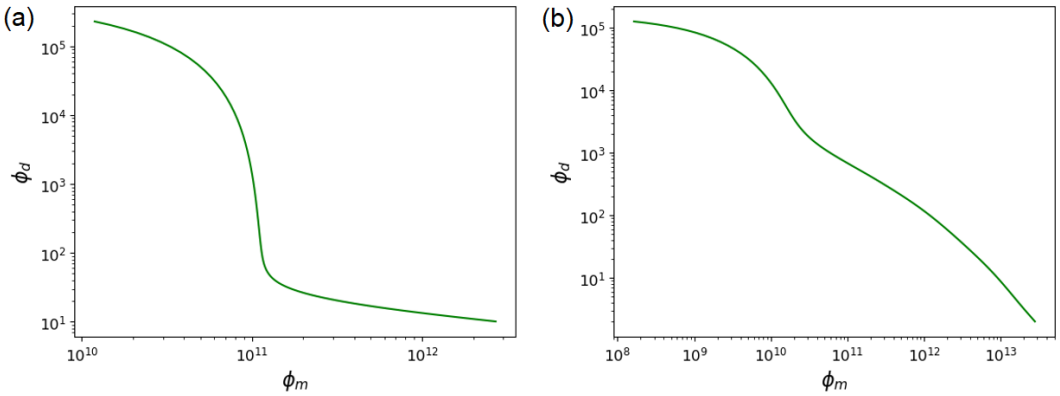

Figure 13. Tikhonov curves constructed from (a) the density contrast equivalent source layers and (b) the susceptibility equivalent source layers. Here, ϕ_d represents the data misfit and ϕ_m represents the model regularization.

an appropriate target data misfit. For the TMI data, we take a second approach to estimating the noise levels. Instead of looking at the Tikhonov curve, we look at the residuals computed from the equivalent source layers that were constructed previously. When the regularization parameter is large, the model is unable to fit the data properly (underfits the data) as evidenced by coherent features and clear spatial patterns on the residuals. As the regularization parameter becomes progressively smaller, the residuals show less coherent features and will eventually show mostly random patterns. The data misfit at this point serves as an estimate for the target data misfit. For the TMI data, we estimated a target data misfit of $2,000$ to be most adequate. The residual corresponding to this data misfit value is shown on Figure 12(d). As was the case with gravity data, a standard deviation of 100 nT proved to be an overestimate of the noise level. The standard deviation for the TMI data in this tile should be closer to 32.51 nT. This same process was applied for each of the tiles, resulting in estimated target data misfits that were used for all the inversions. The data misfits and the estimated noise levels for each tile are summarized in Table S1 in the supporting information.

4.4 Joint Inversion

For each tile, we first performed separate inversions of the QUEST gravity and TMI data, mainly to determine the regularization parameters and weight of the coupling function used for joint inversion. For brevity, the results from separate inversions are not shown. The model space was discretized into a mesh of rectangular prisms such that the core cell size was 500 m × 500 m × 500 m. Padding cells of progressively increasing dimensions were added to the edges of the mesh. Topography was fully accounted for in all inversions. For all tiles, the inversion meshes shared the same vertical dimensions; each inversion mesh consisted of 20 core cells in the vertical direction covering a total depth of 10 km. The lateral dimensions of each mesh depended on the lateral dimensions of the corresponding tile. The core areas of the mesh were then merged into a single mesh that covered the entire QUEST survey area. Cells outside the perimeter of the QUEST survey area were discarded for subsequent analyses and visualizations.

For the gravity inversions, we did not impose any bound constraints because we expected that both positive and negative density contrasts would be required to explain the features visible in Figure 10(a). Additionally, physical properties measured by Mitchinson et al. (2013) on rock samples from porphyry deposits in the QUEST survey area show that the bulk densities in the region can range above and below the density ($2.67\,\mathrm{g\,cm^{-3}}$)

used for the terrain correction on the gravity data. As such, we expected to see both negative and positive density contrasts from the gravity inversions.

For the magnetic inversions, we also did not impose any bound constraints as there is remanence in the region. Natural remanent magnetization was measured by Mitchinson et al. (2013) on rock samples from porphyry deposits in the QUEST survey area. Some of the Koenigsberger ratios reported exceeded a value of 1, indicating strong remanence in some of these areas. As such, we did not make the usual assumption of there being no remanence. Instead, for simplicity, we made the assumption that any remanence has a component that is colinear to the present-day Earth's magnetic field. This means that any negative susceptibilities are attributed to remanent magnetizations in the opposite direction of the present-day geomagnetic field, likely due to polarity reversals. We acknowledge that this is a strong assumption and that there are potential limitations to the magnetic inversions due to such assumptions. However, we note that the magnetic inversions had no trouble fitting the observed data to the desired levels even with such assumptions. As such, for purposes of this study, we accept such assumptions as appropriate. We leave the examination of full magnetization vectors for future research.

Horizontal sections at various depths of the jointly inverted density contrast model are shown in Figure 14 and for the susceptibility model in Figure 15. Note that we set the maximum value for the colorbar of the susceptibility model to the 99.9^{th} percentile to better visualize the features in the model, which would not have been visible otherwise. The predicted data computed from the jointly inverted models are shown in Figure 16. Note that we have set the same maximum and minimum values for the colorbar of the predicted TMI data the same way as we did for the observed TMI data in Figure 10(b).

Lastly, we present the crossplot of the jointly inverted susceptibility and density contrast values in Figure 17(b). For comparison, we also present the crossplot of the susceptibility and density contrast values from separate inversions in Figure 17(a). We observe that the crossplot of the jointly inverted values presents clearer structure and patterns. Namely, we see clear linear features extending towards the high densities and high susceptibilities.

4.4.1 Merging the Inverted Models

As described previously, the survey data was divided into several tiles. The inverted models from each tile were then merged to produce a single model for the whole survey area. The tiles were purposely made to overlap with adjacent tiles so as to ensure continuity and prevent potential artifacts that could arise because of the splitting of the data. The models were merged by using an image processing technique called "alpha compositing". Alpha compositing (or alpha blending) is the process of combining two images to create an appearance of smooth transition between the images (Porter & Duff, 1984). It is often used to blend an image on a background or on top of another image. Here, we use the same technique to smoothly merge the inverted models from each tile. The equation that guides alpha blending is given by

$$\mathbf{m_T} = \alpha \mathbf{m_1} + (1 - \alpha)\mathbf{m_2} \tag{3}$$

where $\mathbf{m_T}$ is the vector with the merged model values while $\mathbf{m_1}$ and $\mathbf{m_2}$ are vectors of the overlapping model values. The merging process only applies to the overlapping areas of the models, so it does not require values that are non-overlapping. The value for α is up to the discretion of the user and using a value of 0.5 would be equivalent to an arithmetic mean of the model values. We used a sigmoid function that varies smoothly in a given direction. Additional details of the merging process can be found in the supporting information (Text S1).

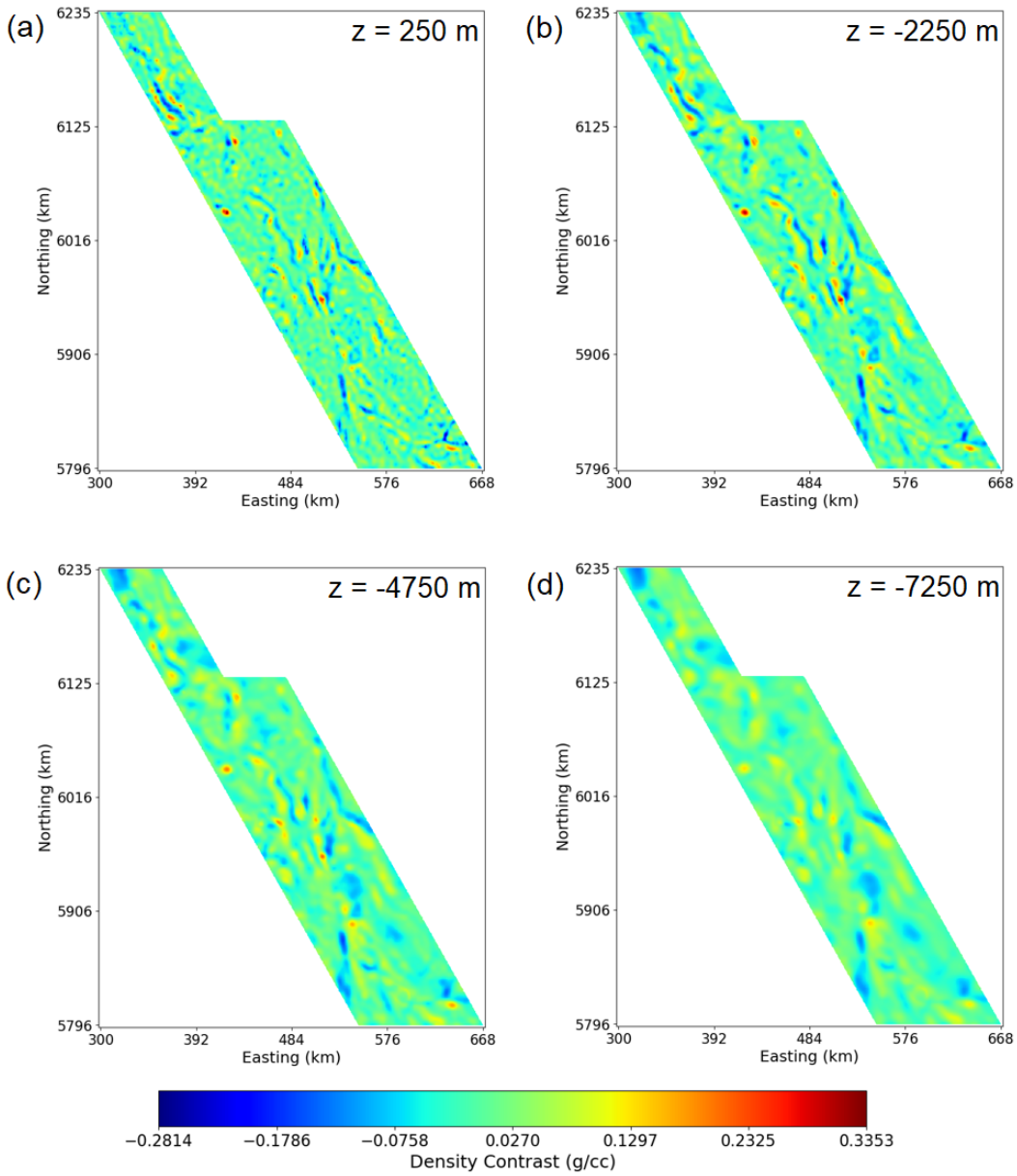

Figure 14. Horizontal sections of the jointly inverted 3D density contrast model at different elevations with respect to sea level.

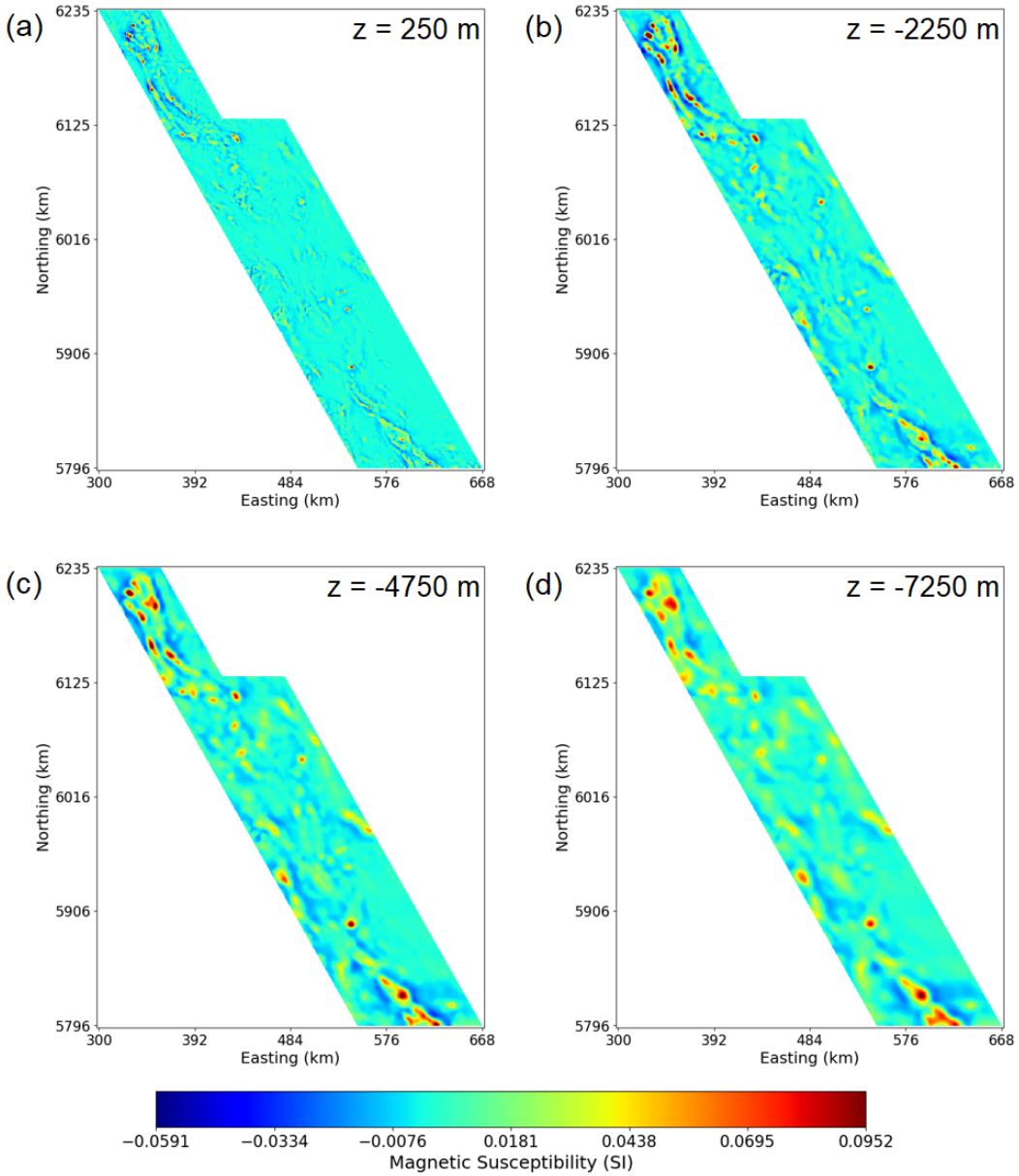

Figure 15. Horizontal sections of the jointly inverted 3D susceptibility model at different elevations with respect to sea level. For better visualization, we set the maximum of the colorbar to the 99.9^{th} percentile.

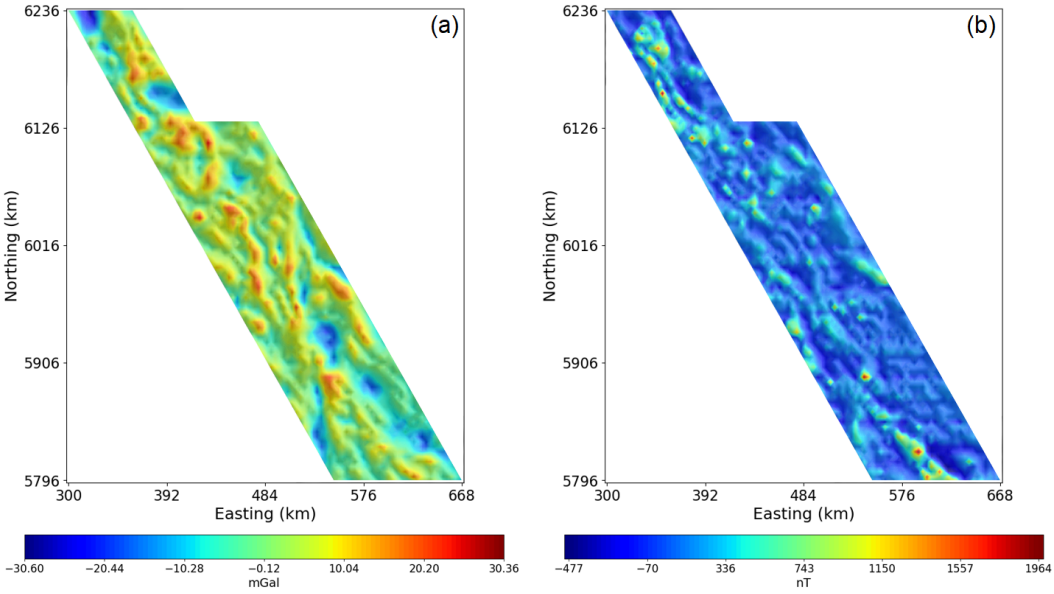

Figure 16. (a) The predicted gravity data from the jointly inverted density contrast model and (b) the predicted TMI data from the jointly inverted susceptibility model.

4.5 Geology Differentiation

Geophysical inversions provide images of the subsurface geological structure in terms of different physical properties. However, effective interpretation of geophysical data, especially in mineral exploration, relies on meaningful inferences for different geological units. The identification of various geological units and their spatial distribution helps guide decision-making in exploration, such as the decisions to drill in specific sites for detailed prospecting of mineral ore deposits. We therefore perform geology differentiation to identify different geological units based on the jointly inverted density contrast and susceptibility values.

Various geological units were identified using BCGS's Digital Geology database (Cui et al., 2017). For simplicity, we have grouped the geological units into larger groups that share common properties. For each geological unit, we defined expected ranges of densities and susceptibility values that were based on the descriptions in Cui et al. (2017) and on physical property measurements reported in Mitchinson et al. (2013). We then classified the points on the crossplot of jointly inverted physical property values based on the expected ranges as well as on the natural trends present on the crossplot as shown in Figure 18. The resulting quasi-geology model is shown in Figure 19. In the following paragraphs, we discuss each of the classes, but for brevity, we only show figures of a few classes with clear features that are correlated with known geology.

We have identified class 1 as mafic intrusions associated with the Hogem Plutonic Suite to the north with a high magnetite content as evidenced by the high susceptibilities (see Figure S7 in the supporting information).

Class 2 we have identified as ultramafic rocks with a higher density range than class 1 that are associated with ore-related potassic alteration mineral assemblages that contain magnetite (Figure 20). Some of the intrusions of this class are spatially correlated with intrusions that are adjacent to the Mount Milligan and Kwanika deposits. Thus, we identify class 2 as a class of interest that is associated with some of the Cu-Au porphyry deposits of the region. To the south, we observe features of class 2 adjacent to the

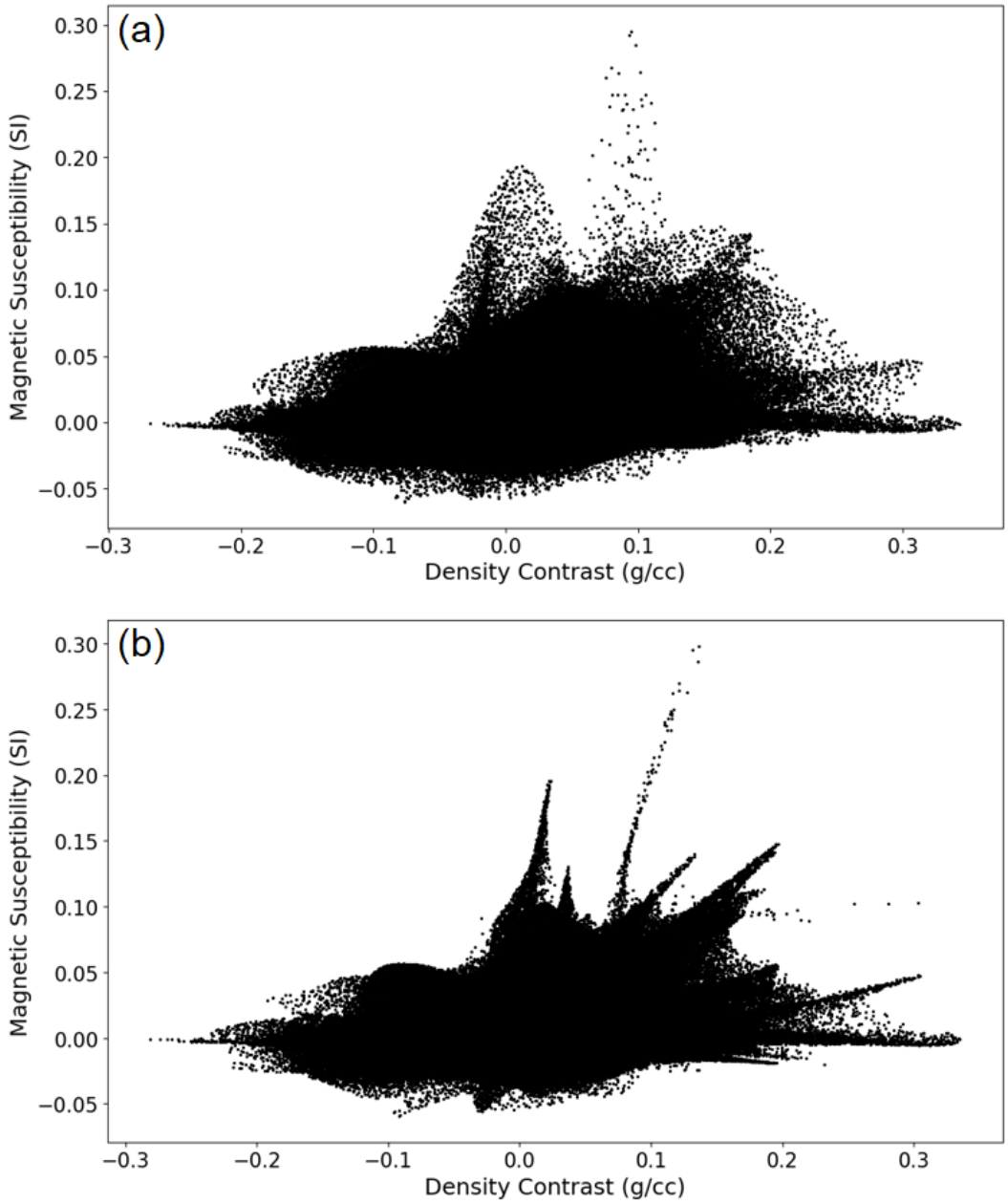

Figure 17. (a) Crossplot of separately inverted susceptibility and density contrast values. (b) Crossplot of jointly inverted susceptibility and density contrast values. Each point in the plots represents one model cell.

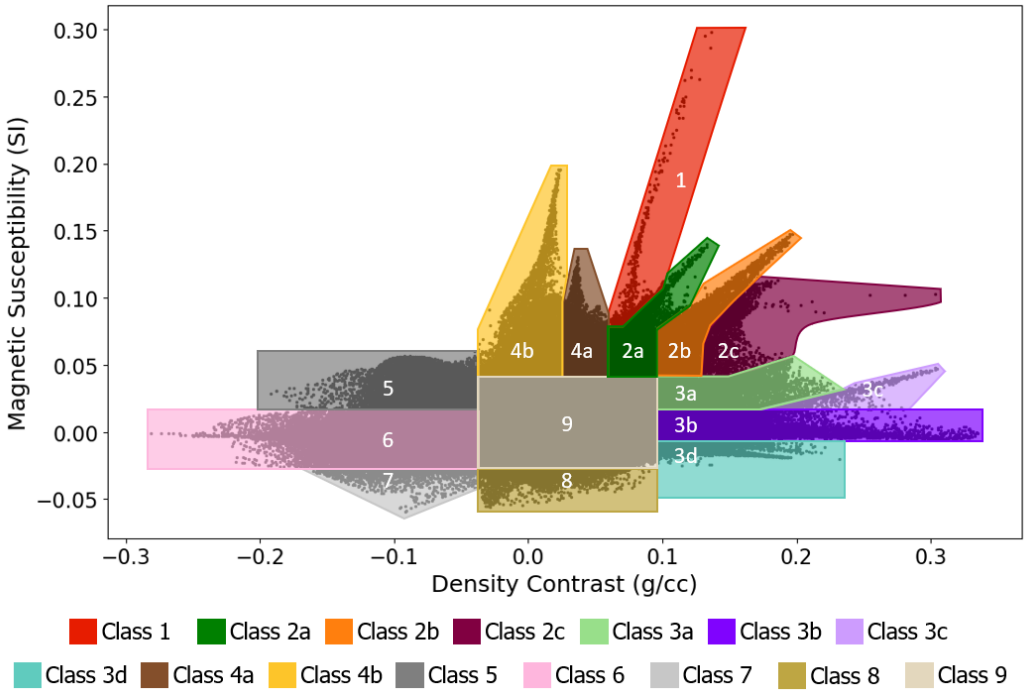

Figure 18. Classification applied to the crossplot of jointly inverted susceptibility and density contrast values.

Polaris Plutonic Suite. Joint inversion allowed us to differentiate class 2 into three subclasses which likely represent differing degrees of alteration and composition: subclass 2a has relatively high susceptibilities but lower densities and is associated to the west with the Trembleur Ultramafites, subclass 2b has similar susceptibilities to subclass 2a but has higher densities, and subclass 2c has lower susceptibilities but extends to higher densities.

Class 3, with low susceptibilities but high densities, is likely to be intermediate to mafic rocks as evidenced by the high densities but with low susceptibilities that could be associated with secondary alteration. As in class 2, class 3 is spatially correlated with intrusions of some of the known Cu-Au porphyry deposits (e.g. Mount Milligan deposit). Joint inversion allowed us to differentiate class 3 into four different subclasses. Subclass 3a ranges from intermediate to high densities with low susceptibilities and is spatially correlated with the Lorraine, Takla-Rainbow, Kwanika, and Mount Milligan deposits to the north and ultramafic units to the south (Figure 21). There is also a significant feature of subclasses 3a and 3b that is located near the Quesnel lake. Subclass 3b has a higher range of densities than subclass 3a but with susceptibilities near zero and is spatially distributed through most of the central part of the survey area. To the north, both subclasses 3a and 3b are likely associated with the Hogem Plutonic Suite, but subclass 3b includes features to the west that are spatially correlated with the Trembleur Ultramafites. Subclass 3c is likely an extension of subclass 3b with higher magnetic content as evidenced by the higher susceptibilites. Subclass 3d is also likely to be an extension of subclass 3b that extends to negative susceptibilities as a result of the smooth regularization on the inversions. There is the possibility that subclass 3d constitutes a separate domain with reversed magnetic polarity but we think that it is unlikely as the values are relatively small in magnitude. Class 3 is of particular interest because it is present under the Quaternary sediment overburden, and thus, may serve as a guide for subsequent detailed sur-

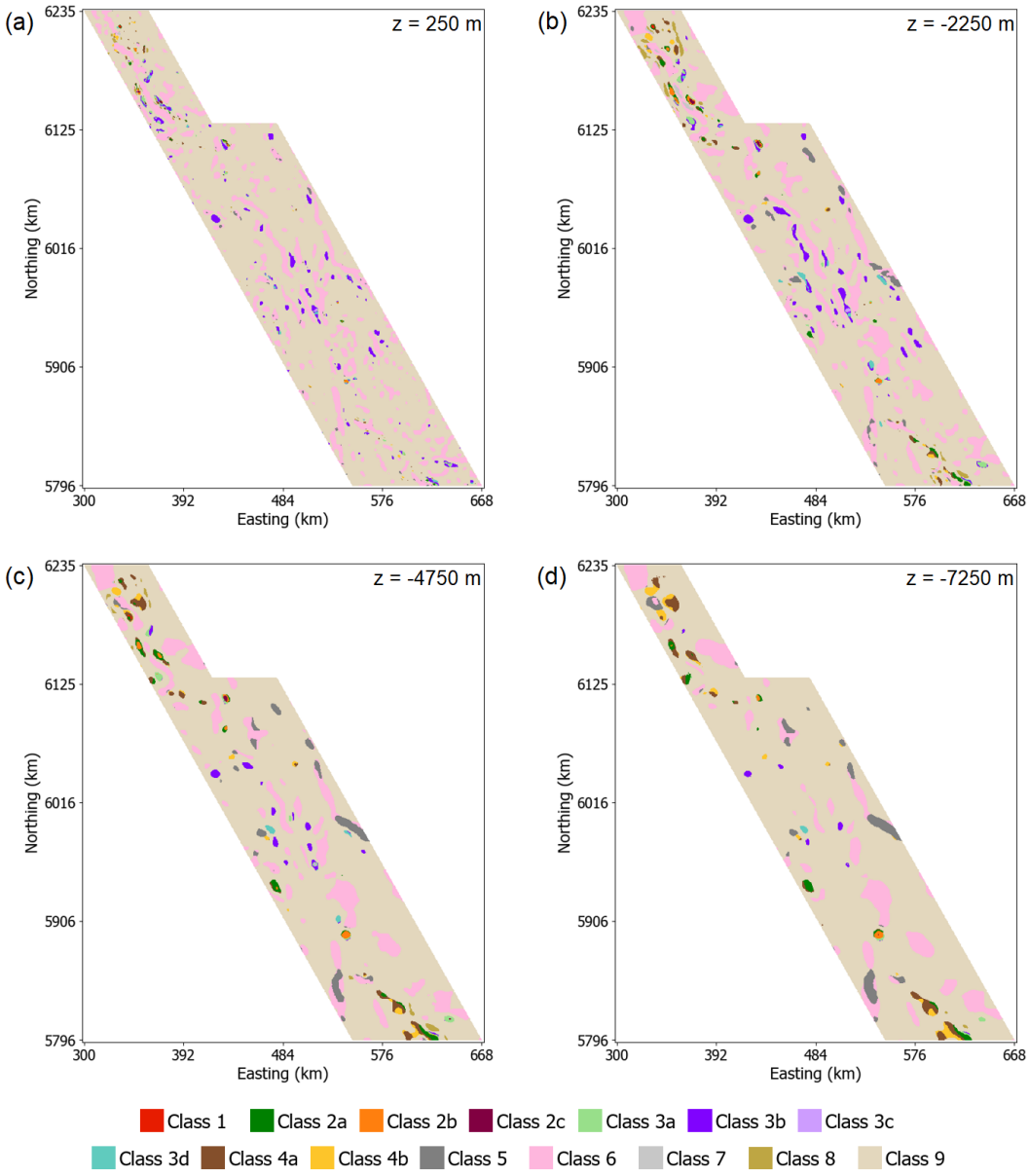

Figure 19. Horizontal sections of the 3D quasi-geology model obtained from geology differentiation at different elevations with respect to sea level.

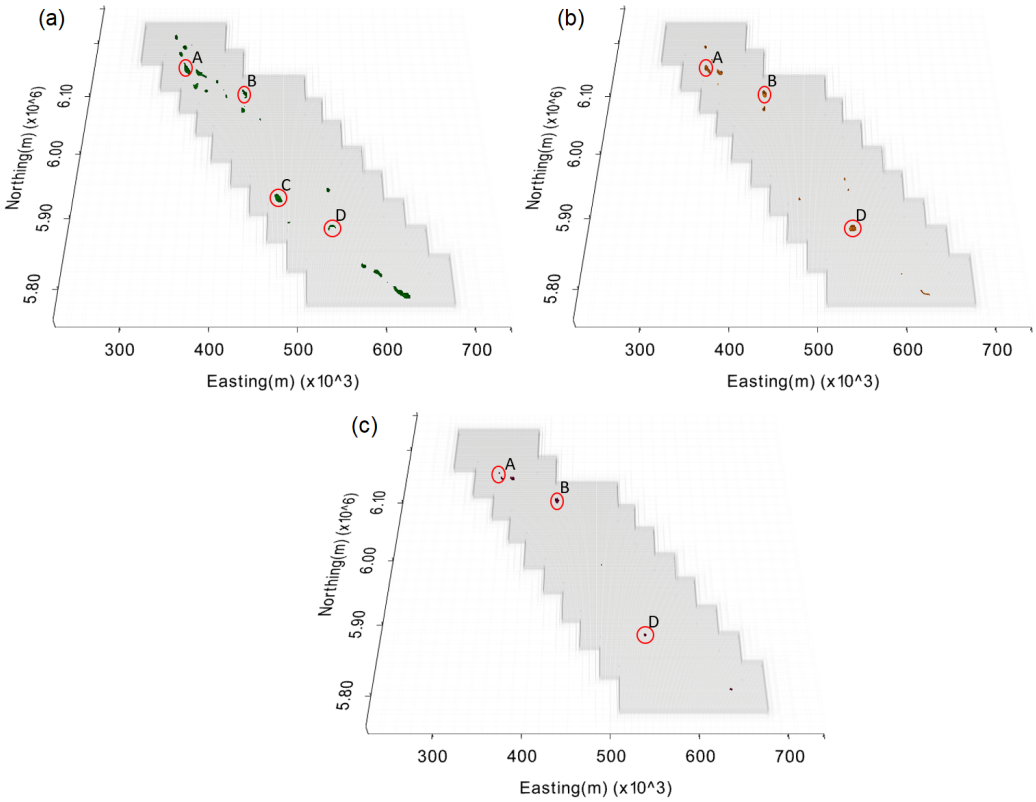

Figure 20. 3D spatial distribution of (a) subclass 2a, (b) subclass 2b, and (c) subclass 2c. Shown in red ellipses are known mineral ore deposits or known geological units: (A) Kwanika deposit, (B) Mount Milligan deposit, (C) Trembleur Ultramafites, (D) Polaris Plutonic Suite.

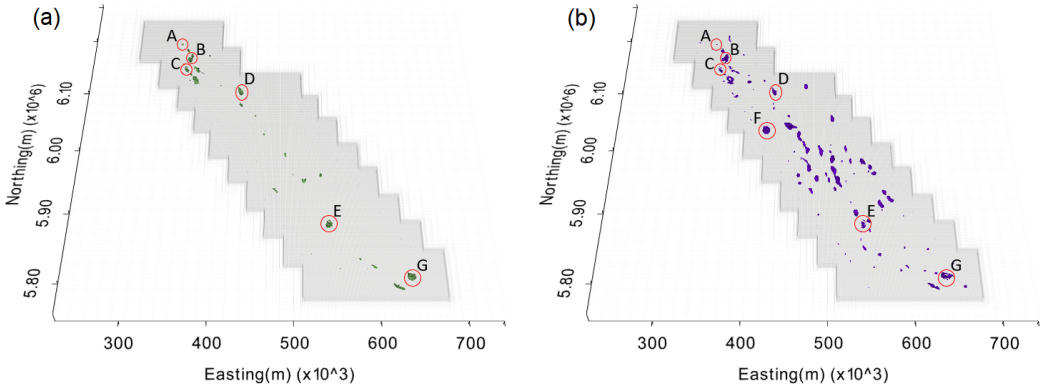

Figure 21. 3D spatial distribution of (a) subclass 3a and (b) subclass 3b. Shown in red ellipses are known mineral ore deposits or known geological units: (A) Lorraine deposit, (B) Takla-Rainbow deposit, (C) Kwanika deposit, (D) Mount Milligan deposit, (E) Polaris Plutonic Suite, (F) Trembleur Ultramafites, (G) Quesnel Lake.

veys around that area. It is worth noting here that previous work on the region shows that some of the mineralization in the region, such as in the Mount Milligan deposit, are associated with phyllic or argillic alteration phases that consumed magnetite leading to lower magnetic susceptibilities (Oldenburg et al., 1997), and thus some of the features with lower magnetic susceptibilities may be associated with mineralization in the region. It is likely that classes 2 and 3 represent different hydrothermal alteration halos, class 2 being associated with early-stage potassic alteration and class 3 with late-stage phyllic alteration (DeLong et al., 1990; Oldenburg et al., 1997; Jago et al., 2014).

Class 4, with near-zero density contrasts but high susceptibilities, are likely granitic intrusions that are associated with the Hogem Plutonic Suite (Ootes et al., 2019) to the north and part of the Mounty Polley complex to the south (see Figure S8 in the supporting information). It is known that the Mount Polley deposit is hosted in an area where the Nicola group volcanics are strongly magnetic, and evidently, subclass 4b, with very high susceptibilities, is spatially correlated with the Mount Polley complex. Subclass 4a is most probably an extension of subclass 4b with less magnetite content but higher densities.

Class 5 is likely to be felsic intrusions that are well distributed throughout the survey area (see Figure S9 in the supporting information). Class 5 is spatially correlated with the Wolverine Metamorphic Complex to the east and the Granite Mountain Batholith to the south, which is the host to the Gibraltar deposit. Due to the weakly magnetic Granite Mountain Batholith, the Gibraltar deposit is indistinguishable from the weakly magnetic rocks that form class 5.

Class 6 is widely distributed throughout the survey area and has low densities and near-zero susceptibilities, suggesting that it could likely be silicic intrusions. Class 6 is spatially correlated with the Hogem Plutonic Suite and the Germansen Batholith in the north and the Bayonne Plutonic Suite in the central region (Figure 22). Class 6 is particularly remarkable as the shape of the resolved Germansen Batholith and Bayonne Plutonic Suite closely resemble the geologic map compiled by Cui et al. (2017) (Figure 23).

Class 7 is sparsely distributed mostly in the north and is likely a felsic extension of the Hogem Plutonic Suite with reversed magnetic polarities as evidenced by the negative susceptibility values (see Figure S10 in the supporting information). We note that

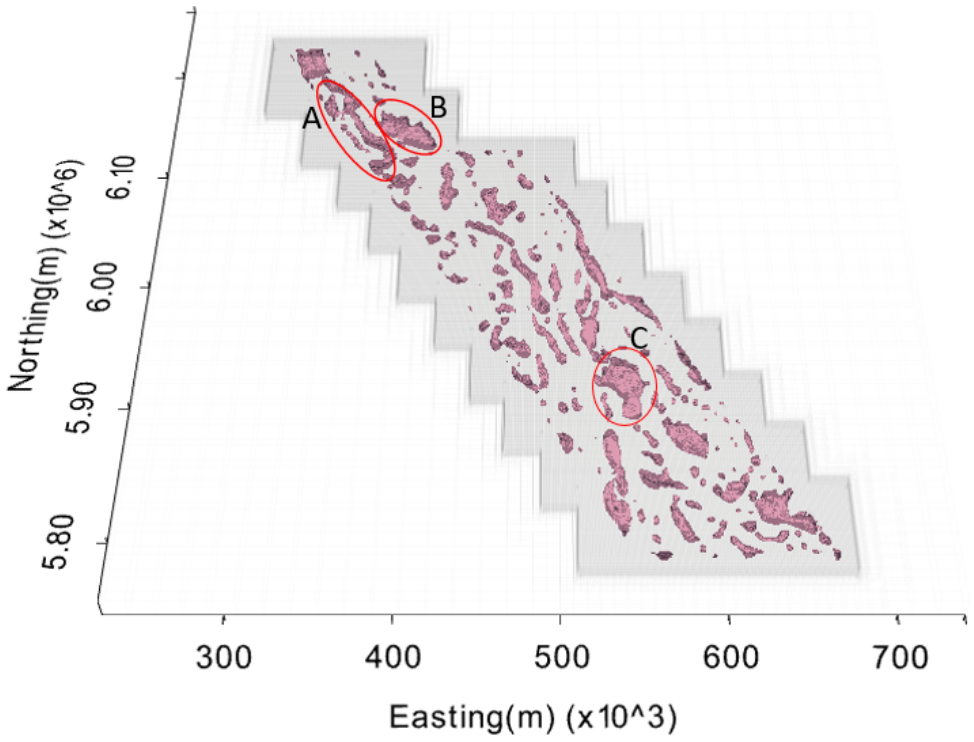

Figure 22. 3D spatial distribution of class 6. Shown in red ellipses are known geological units: (A) Hogem Plutonic Suite, (B) Germansen Batholith, (C) Bayonne Plutonic Suite.

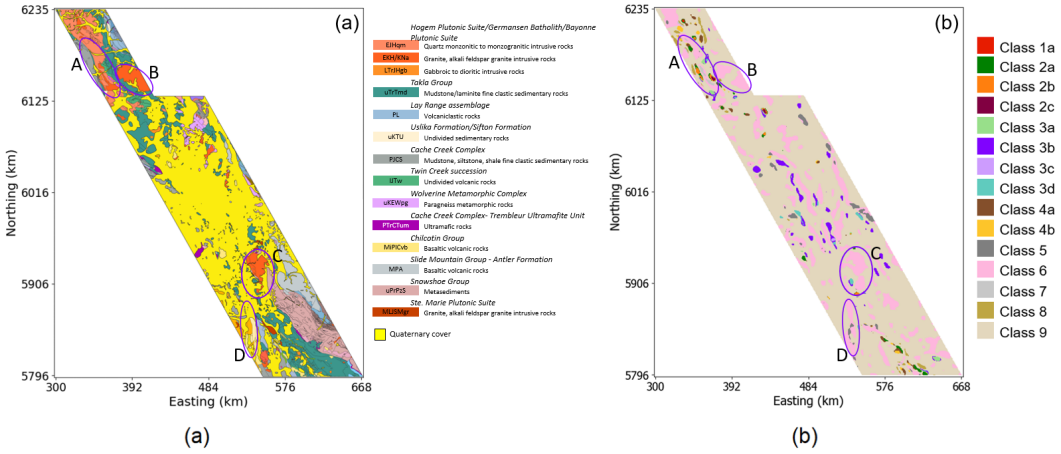

Figure 23. (a) Geological map of the QUEST survey area, adopted from (Cui et al., 2017) (note only the most representative units are presented on the legend), and (b) Horizontal section of the 3D quasi-geology model shown at elevation $z = -2250$ m. Shown in purple ellipses are known geological units: (A) Hogem Plutonic Suite, (B) Germansen Batholith, (C) Bayonne Plutonic Suite, (D) Australian Creek, Fraser Bend and Crownite formations. The locations and shapes of these units are nearly identically represented on both the geological map on the left and the 3D quasi-geology model on the right.

the negative susceptibilities for class 7 range to larger magnitudes, suggesting that it is more likely to be a result of polarity reversals rather than of smoothing regularization.

Class 8, with near-zero density contrasts but negative susceptibilities with relatively high magnitude, are likely granitic intrusions similar to class 4, but with reversed polarities (see Figure S11 in the supporting information). Class 4 likely formed during a period of normal magnetic polarity, while class 8 could have been formed during a magnetic reversal period.

Class 9 is widely distributed throughout the survey area and likely constitutes a wide range of rock types ranging from sedimentary to felsic and intermediate volcanic rocks that represent the host rock of the Quesnel terrane (see Figure S12 in the supporting information). It is worth noting that class 9 extends to negative susceptibilities but the relatively low magnitudes suggest that this is likely a result of the smooth regularization of the inversions.

Lastly, we show a comparison of the 2D geological map modified from Cui et al. (2017) and our 3D quasi-geology model in Figure 23. The correspondence between the two figures is most apparent to the north and south where the structure of the quasi-geology model on the right closely resembles the geologic map on the left. The 3D quasi-geology model is able to further differentiate the geology in more detail in the central region of the survey area and it also adds a third dimension, depth, to the geological interpretation.

4.6 Discussions

An application of the quantitative workflow for the integrated interpretation of multiple geophysical and geological data was presented in this study. Integration of multiple geophysical data sets was performed through joint inversion that enhances structural similarity between the different physical property models. Integration with geological information was performed through a process of geology differentiation based on prior geological knowledge and inverted physical property values. The application of the workflow to the QUEST gravity and TMI data allowed us to distinguish and differentiate various geological units, some of which are spatially correlated with known mineral ore deposits or geological features.

Finally, as a recommendation for future studies, we have identified areas in the central portion and in the south of the QUEST survey area where more detailed surveys may provide a better understanding of the mineral prospectivity in these underexplored areas of the Quesnel terrane. The areas of interest were identified by combining subclasses 2a, 2b, 3a, and 3b from the geology differentiation applied on the jointly inverted physical property values. Subclasses 2a and 2b were correlated with intrusions with high magnetic content. Subclasses 3a and 3b corresponded to mafic rocks that were spatially correlated with the Trembleur Ultramafites and other mafic intrusions to the north (Hogem Plutonic Suite). Subclasses 3a and 3b were also spatially correlated with the intrusions associated with the Lorraine, Takla-Rainbow, Kwanika, and Mount Milligan deposits particularly at shallower depths, whereas subclasses 2a and 2b correlated with the deposits on the perimeter, which likely represents a different alteration zone. Most notable, however, is that subclass 3b is spatially distributed throughout the central region under the Quaternary sediment cover where the geological description is lacking. Figure 24 shows in red circles the locations of the correlated deposits, in purple circles the locations of the ultramafic units, and in blue squares areas of interest for future detailed surveys. The large blue square in the middle is an area covered by the Quaternary glacial overburden that lacks detailed geological descriptions and has the potential for new mineral ore deposits. The bottom square is an area close to the Quesnel Lake that has two prominent features belonging to these subclasses in an area that lacks much geological description and could be worth investigating further.

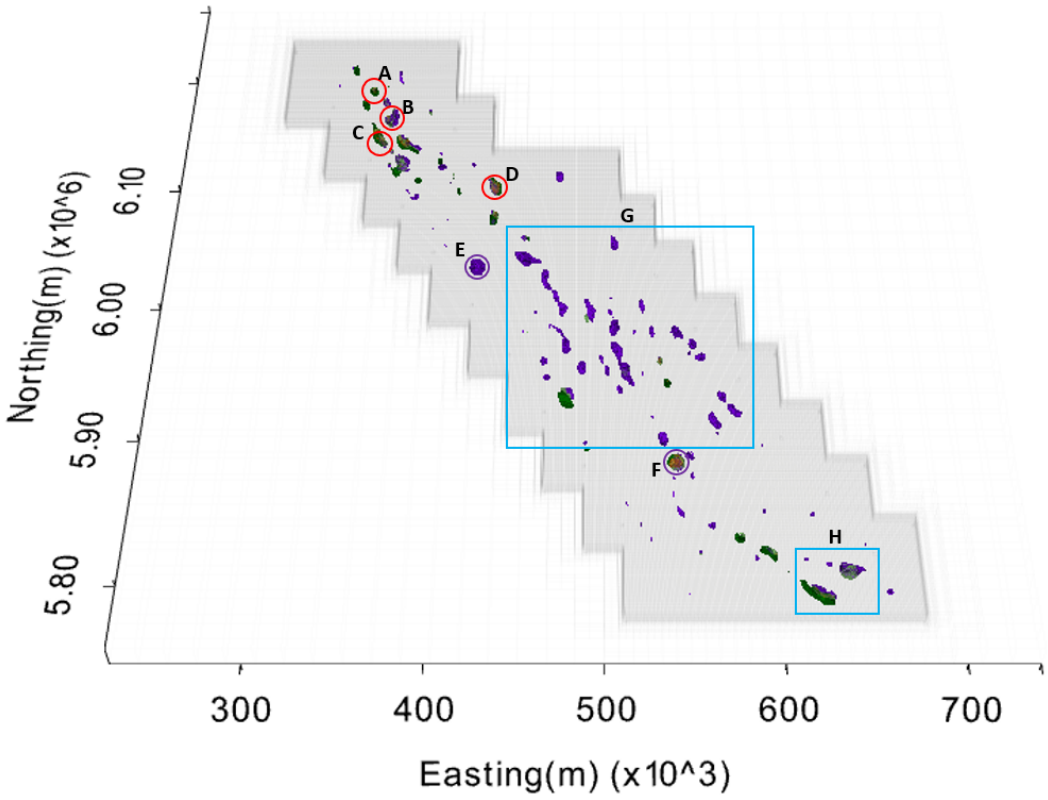

Figure 24. Spatial distribution of subclasses 2a, 2b, 3a, and 3b. Shown in red circles are known mineral deposits: (A) Lorraine, (B) Takla-Rainbow, (C) Kwanika, (D) Mount Milligan deposits. Shown in purple circles are known ultramafic units: (E) Trembleur Ulframafites, (F) Polaris Plutonic Suite. In blue squares are target areas for future detailed surveys as they represent areas where the geological description is lacking and has the potential for mineral deposits: (G) An area that lies beneath the Quaternary glacial overburden, (H) An area that lies south of the survey area near the Quesnel Lake.

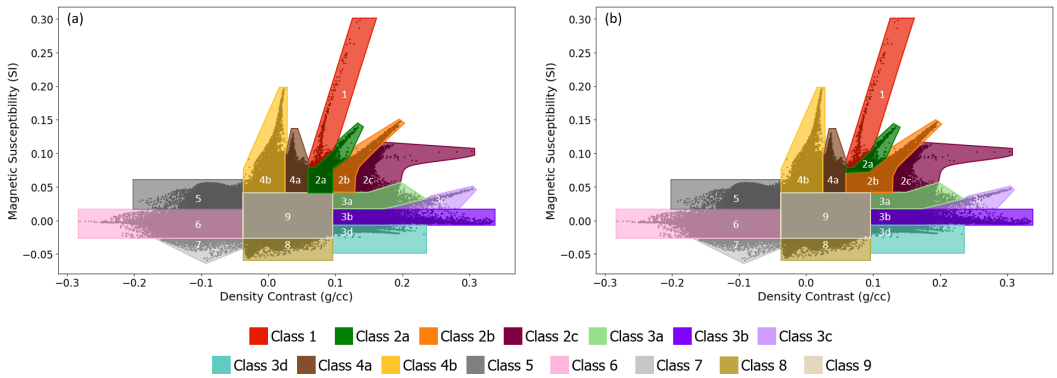

Figure 25. (a) Original classification and (b) alternative classification of the jointly inverted susceptibility and density contrast values. Note that for the alternative classification, subclasses 2a and 2b have changed.

There are other mineral deposits in the QUEST survey area, such as the Gibraltar and Mount Polley deposits, that were not identified on the geology differentiation results at the regional scale of the present work. Mount Polley is hosted in strongly magnetic volcanic host rocks (Logan & Mihalynuk, 2014), likely classified to class 4 in the geology differentiation which makes it hard to differentiate. The Gibraltar deposit is hosted in the weakly magnetic Granite Mountain Batholith (Schiarizza, 2014), which makes it indistinguishable from other weakly magnetic volcanics and host rock.

Finally, we acknowledge the fact that there is a level of subjectivity still involved, particularly in the geology differentiation step where different geological units are identified. The results from the geology differentiation are inferences; borehole information is needed to validate the interpretations. To explore this ambiguity, we have experimented with several different classifications, altering the boundaries between the different classes. As an example, we present a comparison between our original classification and an alternative one (Figure 25). In this case, any of the individual cells lost by subclass 2a will be added to 2b (Figure 26). This, in turn, does not affect our final interpretation when we include both subclasses 2a and 2b in our final recommendation. We also notice that there is greater ambiguity in classes with lower densities, suggesting that there is significant overlap in density and susceptibility values between the felsic and intermediate geological units.

5 Conclusions

Quantitative integration of multiphysics geoscientific data is an active field of research. Joint inversions are of particular interest because they provide quantitative means to integrating multiple geophysical data sets for the construction of physical property models that are consistent with each other. However, interpretation of geophysical inversions has traditionally relied on the identification for anomalous features that are indicative of a target of interest. The work presented here represents a step further in the interpretation of geophysical inversions, employing a geology differentiation method that allows for the further addition of geological knowledge into the interpretation process.

For this study, we combined joint inversion and geology differentiation for the integrated interpretation of multiple geoscientific data sets in mineral exploration. In this study, we performed structural joint inversion using the cross-gradient constraint to produce structurally similar density contrast and susceptibility models. Geology differen-

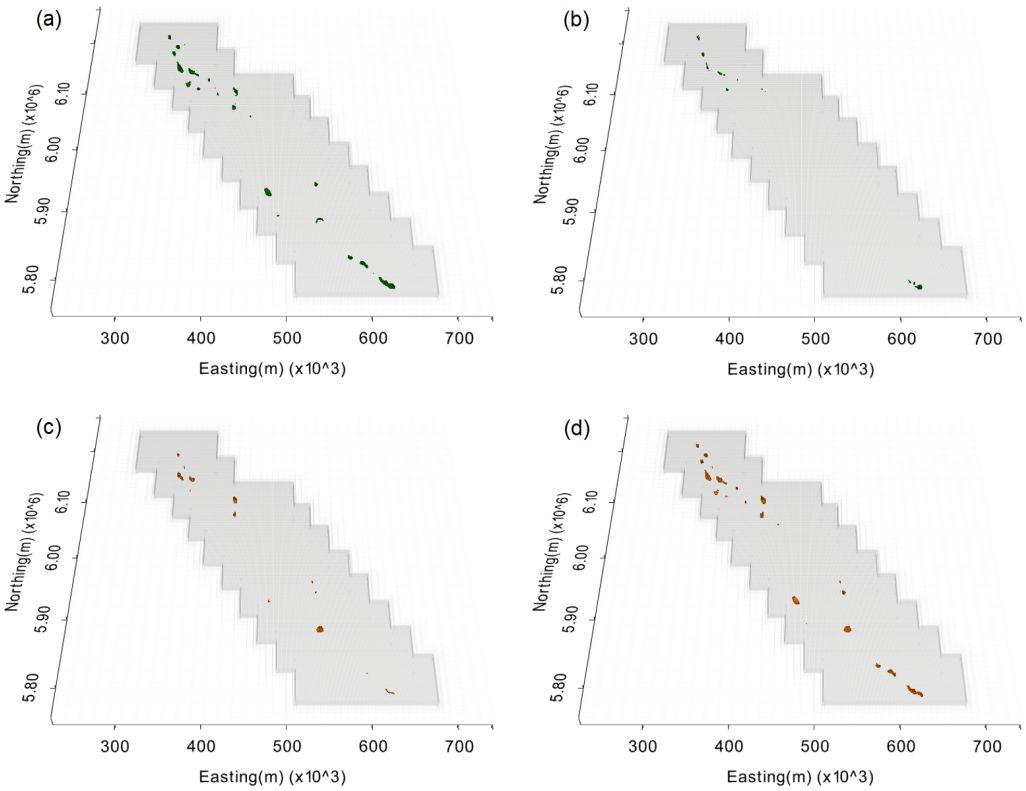

Figure 26. (Top) Subclass 2a from the (a) original and (b) alternative classification. (Bottom) Subclass 2b from the (c) original and (d) alternative classification.

tiation was then applied to the jointly inverted models to identify different geological units. The workflow was validated using synthetic data before being applied to airborne gravity and TMI data from Quesnel terrane in central British Columbia with the purpose of regional-scale mineral exploration. The results showed that geology differentiation based on joint inversion led to a finer distinction between different geological units. This in turn helped identify areas of interest for future detailed surveys. In particular, an area in the central part of the Quesnel terrane that lies beneath the Quaternary sediment overburden was identified as an area of interest for future detailed surveys, as this area showed similar features associated with known mineral deposits (e.g. Mount Milligan, Lorraine deposits). Results from the geology differentiation were validated using geology maps compiled in previous work. Integrated interpretation of multiple geophysical and geological data through joint inversion and geology differentiation shows promise not only for mineral exploration, but also for any other geoscientific study that involves multiple data types.

6 Availability Statement

The airborne gravity and magnetics data are archived and made publicly available by Geoscience BC (`http://www.geosciencebc.com/major-projects/quest/`). Readers can access the airborne gravity data at `http://www.geosciencebc.com/i/project_data/QUESTdata/GBCReport2008-8/GBCReport2008-8_Gravity_Data.zip` and the associated technical report at `http://www.geosciencebc.com/i/project_data/QUESTdata/GBCReport2008-8/Gravity_Technical_Report.pdf`. The airborne magnetic data can be accessed at `http://www.geosciencebc.com/i/project_data/QUESTdata/maps_geosoft_viewer/Mag2_Main.zip`. The report pertaining to magnetic data can be accessed at `http://www.geosciencebc.com/i/project_data/QUESTdata/report/7042-GeoscienceBC_final.pdf`. The joint inversion code that was used to invert the geophysical data is available at `https://github.com/xiaolongw1223`.

7 acknowledgments

We wish to thank Geoscience BC for making the field data from the QUEST project available, SimPEG for the separate inversion codes, PyVista for the visualization codes, and the Hewlett Packard Enterprise Data Science Institute at the University of Houston for providing the computing resources used for this research.

References

Afnimar, Koketsu, K., & Nakagawa, K. (2002, October). Joint inversion of refraction and gravity data for the three-dimensional topography of a sediment–basement interface. *Geophysical Journal International*, *151*(1), 243–254. Retrieved 2021-09-08, from `https://doi.org/10.1046/j.1365-246X.2002.01772.x` doi: 10.1046/j.1365-246X.2002.01772.x

Astic, T., Fournier, D., & Oldenburg, D. W. (2020, November). Joint inversion of potential-fields data over the DO-27 kimberlite pipe using a Gaussian mixture model prior. *Interpretation*, *8*(4), SS47–SS62. Retrieved 2021-09-08, from `https://library.seg.org/doi/full/10.1190/INT-2019-0283.1` (Publisher: Society of Exploration Geophysicists) doi: 10.1190/INT-2019-0283.1

Cockett, R., Kang, S., Heagy, L. J., Pidlisecky, A., & Oldenburg, D. W. (2015). SimPEG: An open source framework for simulation and gradient based parameter estimation in geophysical applications. *Computers & Geosciences*, *85*, 142–154. Retrieved from `http://www.sciencedirect.com/science/article/pii/S009830041530056X` doi: https://doi.org/10.1016/j.cageo.2015.09.015

Cui, Y., Miller, D., Schiarizza, P., & Diakow, L. (2017). *British Columbia digital geology. British Columbia Ministry of Energy, Mines and Petroleum Resources,*

British Columbia Geological Survey Open File 2017-8, 9p. Data version 2019-12-19. British Columbia Ministry of Energy, Mines and Petroleum Resources. Retrieved from https://www2.gov.bc.ca/gov/content/industry/mineral-exploration-mining/british-columbia-geological-survey/geology/bcdigitalgeology (Pages: 9 Place: British Columbia Geological Survey Open File 2017-8, 9p. Data version 2019-12-19.)

Dampney, C. N. G. (1969). The Equivalent Source Technique. *GEOPHYSICS*, *34*(1), 39–53. Retrieved from https://doi.org/10.1190/1.1439996 doi: 10.1190/1.1439996

DeLong, R., Godwin, C., Harris, M., Caira, N., & Rebagliati, C. (1990, January). GEOLOGY AND ALTERATION AT THE MOUNT MILLIGAN GOLD-COPPER PORPHYRY DEPOSIT, CENTRAL BRITISH COLUMBIA (93N/lE).

Doetsch, J., Linde, N., Coscia, I., Greenhalgh, S. A., & Green, A. G. (2010a). Zonation for 3D aquifer characterization based on joint inversions of multimethod crosshole geophysical data. *Geophysics*, *75*(6), G53-G64.

Doetsch, J., Linde, N., Coscia, I., Greenhalgh, S. A., & Green, A. G. (2010b). Zonation for 3D aquifer characterization based on joint inversions of multimethod crosshole geophysical data. *GEOPHYSICS*, *75*(6), G53–G64. Retrieved from https://doi.org/10.1190/1.3496476 doi: 10.1190/1.3496476

Farr, A., Meyer, S., & Bates, M. (2008). *Airborne Gravity Survey Quesnellia Region, British Columbia 2008* (Tech. Rep.). Ottawa: Sander Geophysics Limited. Retrieved from http://www.geosciencebc.com/reports/gbcr-2008-08/

Fraser, S. J., Wilson, G. A., Cox, L. H., Čuma, M., Zhdanov, M. S., & Vallée, M. A. (2012). Self-organizing maps for pseudo-lithological classification of 3D airborne electromagnetic, gravity gradiometry and magnetic inversions. *ASEG Extended Abstracts*, *2012*(1), 1–4. Retrieved from https://doi.org/10.1071/ASEG2012ab086 (Publisher: Taylor & Francis) doi: 10.1071/ASEG2012ab086

Fregoso, E., & Gallardo, L. A. (2009a). Cross-gradients joint 3D inversion with applications to gravity and magnetic data. *Geophysics*, *74*(4), L31-L42. doi: 10.1190/1.3119263

Fregoso, E., & Gallardo, L. A. (2009b). Cross-gradients joint 3D inversion with applications to gravity and magnetic data. *GEOPHYSICS*, *74*(4), L31–L42. Retrieved from https://doi.org/10.1190/1.3119263 doi: 10.1190/1.3119263

Gallardo, L. A., & Meju, M. A. (2003). Characterization of heterogeneous near-surface materials by joint 2D inversion of dc resistivity and seismic data. *Geophysical Research Letters*, *30*(13). Retrieved from https://agupubs.onlinelibrary.wiley.com/doi/abs/10.1029/2003GL017370 doi: 10.1029/2003GL017370

Geoscience BC. (2008). *Geoscience BC summary of activities 2007* (Tech. Rep.). Geoscience BC, Report 2008-1, 150 p. Retrieved from http://www.geosciencebc.com/major-projects/quest/ (Publication Title: QUEST)

Geotech Ltd. (2008). *Report on a Helicopter-Borne Versatile Time Domain Electromagnetic (VTEM) Geophysical Survey* (Tech. Rep.). Aurora: Geotech Ltd. Retrieved from http://www.geosciencebc.com/reports/gbcr-2008-04/

Goodwin, J. A., & Skirrow, R. G. (2019). Mapping IOCG-related alteration using 3D gravity and magnetic inversion: an example from the Tennant Creek – Mount Isa region, northern Australia. *ASEG Extended Abstracts*, *2019*(1), 1–6. Retrieved from https://doi.org/10.1080/22020586.2019.12073080 (Publisher: Taylor & Francis) doi: 10.1080/22020586.2019.12073080

Hanneson, J. E. (2003). On the use of magnetics and gravity to discriminate between gabbro and iron-rich ore-forming systems. *Exploration Geophysics*, *34*(1-2), 110–113. Retrieved from https://doi.org/10.1071/EG03110 (Publisher:

Taylor & Francis) doi: 10.1071/EG03110

Hansen, P. C., & O'Leary, D. P. (1993). The Use of the L-Curve in the Regularization of Discrete Ill-Posed Problems. *SIAM Journal on Scientific Computing*, *14*(6), 1487–1503. Retrieved from https://doi.org/10.1137/0914086 doi: 10.1137/0914086

Infante, V., Gallardo, L. A., Montalvo-Arrieta, J. C., & de León, I. N. (2010). Lithology classification assisted by joint inversion of electrical and seismic data at a control site in northeast Mexico. *Journal of Applied Geophysics*, *70*, 93-102.

Jago, C. P., Tosdal, R. M., Cooke, D. R., & Harris, A. C. (2014, June). Vertical and Lateral Variation of Mineralogy and Chemistry in the Early Jurassic Mt. Milligan Alkalic Porphyry Au-Cu Deposit, British Columbia, Canada*. *Economic Geology*, *109*(4), 1005–1033. Retrieved 2021-09-13, from https://doi.org/10.2113/econgeo.109.4.1005 doi: 10.2113/econgeo.109.4.1005

Kamm, J., Lundin, I. A., Bastani, M., Sadeghi, M., & Pedersen, L. B. (2015, September). Joint inversion of gravity, magnetic, and petrophysical data — A case study from a gabbro intrusion in Boden, Sweden. *GEOPHYSICS*, *80*(5), B131–B152. Retrieved 2021-09-08, from https://library.seg.org/doi/full/10.1190/geo2014-0122.1 (Publisher: Society of Exploration Geophysicists) doi: 10.1190/geo2014-0122.1

Kowalczyk, P., Oldenburg, D. W., Phillips, N., Nguyen, T. N. H., & Thomson, V. (2010). Acquisition and analysis of the 2007-2009 Geoscience BC airborne data. In R. Lane (Ed.), *Airborne Gravity 2010 - Abstracts from the ASEG-PESA Airborne Gravity 2010 Workshop* (pp. 115–124). Canberra: Geoscience Australia and the Geological Survey of New South Wales.

Lelièvre, P. G., Farquharson, C. G., & Hurich, C. A. (2012). Joint inversion of seismic traveltimes and gravity data on unstructured grids with application to mineral exploration. *GEOPHYSICS*, *77*(1), K1–K15. Retrieved from https://doi.org/10.1190/geo2011-0154.1 doi: 10.1190/geo2011-0154.1

Li, K., Wei, X., & Sun, J. (2021, September). Geophysical characterization of a buried niobium and rare earth element deposit using 3D joint inversion and geology differentiation: A case study on the Elk Creek carbonatite. In *First International Meeting for Applied Geoscience & Energy Expanded Abstracts* (pp. 1256–1260). Society of Exploration Geophysicists. Retrieved 2021-09-08, from https://library.seg.org/doi/10.1190/segam2021-3585069.1 doi: 10.1190/segam2021-3585069.1

Li, X., & Sun, J. (2021, September). Understanding the recoverability of physical property relationships from geophysical inversions of multiple potential-field data sets. In *First International Meeting for Applied Geoscience & Energy Expanded Abstracts* (pp. 1236–1240). Society of Exploration Geophysicists. Retrieved 2021-09-09, from https://library.seg.org/doi/abs/10.1190/segam2021-3594791.1 doi: 10.1190/segam2021-3594791.1

Li, Y., Melo, A., Martinez, C., & Sun, J. (2019). Geology differentiation: A new frontier in quantitative geophysical interpretation in mineral exploration. *The Leading Edge*, *38*(1), 60–66. Retrieved from https://doi.org/10.1190/tle38010060.1 doi: 10.1190/tle38010060.1

Li, Y., & Oldenburg, D. W. (1996). 3-D inversion of magnetic data. *Geophysics*, *61*. doi: 10.1190/1.1443968

Li, Y., & Oldenburg, D. W. (1998a). 3-D inversion of gravity data. *GEOPHYSICS*, *63*(1), 109–119. Retrieved from https://doi.org/10.1190/1.1444302 doi: 10.1190/1.1444302

Li, Y., & Oldenburg, D. W. (1998b). Separation of regional and residual magnetic field data. *GEOPHYSICS*, *63*(2), 431–439. Retrieved from https://doi.org/10.1190/1.1444343 doi: 10.1190/1.1444343

Li, Y., & Oldenburg, D. W. (2000). Joint inversion of surface and three-component

borehole magnetic data. *GEOPHYSICS*, *65*(2), 540–552. Retrieved from https://doi.org/10.1190/1.1444749 doi: 10.1190/1.1444749

Linde, N., Binley, A., Tryggvason, A., Pedersen, L. B., & Revil, A. (2006). Improved hydrogeophysical characterization using joint inversion of cross-hole electrical resistance and ground-penetrating radar traveltime data. *Water Resources Research*, *42*(12). Retrieved from https://agupubs.onlinelibrary.wiley.com/doi/abs/10.1029/2006WR005131 doi: 10.1029/2006WR005131

Linde, N., Tryggvason, A., Peterson, J. E., & Hubbard, S. S. (2008). Joint inversion of crosshole radar and seismic traveltimes acquired at the South Oyster Bacterial Transport Site. *GEOPHYSICS*, *73*(4), G29–G37. Retrieved from https://doi.org/10.1190/1.2937467 doi: 10.1190/1.2937467

Logan, J. M., & Mihalynuk, M. G. (2014). Tectonic Controls on Early Mesozoic Paired Alkaline Porphyry Deposit Belts (Cu-Au ± Ag-Pt-Pd-Mo) Within the Canadian Cordillera. *Economic Geology*, *109*(4), 827–858. Retrieved from https://doi.org/10.2113/econgeo.109.4.827 doi: 10.2113/econgeo.109.4.827

Martinez, C., & Li, Y. (2015). Lithologic characterization using airborne gravity gradient and aeromagnetic data for mineral exploration: A case study in the Quadrilátero Ferrífero, Brazil. *Interpretation*, *3*(2), SL1–SL13. Retrieved from https://doi.org/10.1190/INT-2014-0195.1 doi: 10.1190/INT-2014-0195.1

Melo, A., & Li, Y. (2016). Geological characterization applying k-means clustering to 3D magnetic, gravity gradient, and DC resistivity inversions: A case study at an iron oxide copper gold (IOCG) deposit. In *SEG Technical Program Expanded Abstracts 2016* (pp. 2180–2184). Retrieved from https://library.seg.org/doi/abs/10.1190/segam2016-13863735.1 doi: 10.1190/segam2016-13863735.1

Melo, A. T., & Li, Y. (2019). Geology differentiation of geophysical inversions using machine learning. In *International Workshop on Gravity, Electrical & Magnetic Methods and Their Applications, Xi'an, China, 19–22 May 2019* (pp. 301–304). Retrieved from https://library.seg.org/doi/abs/10.1190/GEM2019-076.1 doi: 10.1190/GEM2019-076.1

Melo, A. T., Sun, J., & Li, Y. (2017). Geophysical inversions applied to 3D geology characterization of an iron oxide copper-gold deposit in Brazil. *GEOPHYSICS*, *82*(5), K1–K13. Retrieved from https://doi.org/10.1190/geo2016-0490.1 doi: 10.1190/geo2016-0490.1

Mitchinson, D., Enkin, R., & Hart, C. (2013). *Linking Porphyry Deposit Geology to Geophysics via Physical Properties: Adding Value to Geoscience BC Geophysical Data* (Tech. Rep.). Vancouver: University of British Columbia - MDRU. Retrieved from http://www.geosciencebc.com/reports/gbcr-2013-14/

Moorkamp, M., Lelièvre, P. G., Linde, N., & Khan, A. (2016). Integrated Imaging of the Earth. In *Integrated Imaging of the Earth* (pp. 1–6). AGU. Retrieved from https://agupubs.onlinelibrary.wiley.com/doi/abs/10.1002/9781118929063.ch1 (Section: 1) doi: 10.1002/9781118929063.ch1

Oldenburg, D. W., & Li, Y. (2005). Inversion for Applied Geophysics: A Tutorial. In *Near-Surface Geophysics*. Society of Exploration Geophysicists. Retrieved from https://doi.org/10.1190/1.9781560801719.ch5 doi: 10.1190/1.9781560801719.ch5

Oldenburg, D. W., Li, Y., & Ellis, R. G. (1997). Inversion of geophysical data over a copper gold porphyry deposit: A case history for Mt. Milligan. *GEOPHYSICS*, *62*(5), 1419–1431. Retrieved from https://doi.org/10.1190/1.1444246 doi: 10.1190/1.1444246

Ootes, L., Bergen, A., Milidragovic, D., Graham, B., & Simmonds, R. (2019). *Preliminary geology of northern Hogem batholith, Quesnel terrane, north-central British Columbia.* Retrieved 2021-09-13, from https://www.semanticscholar

.org/paper/Preliminary-geology-of-northern-Hogem-batholith%2C-Ootes-Bergen/20d5d87c7490eee89f81f2b4d73089aa1bf76627

Phillips, N., Nguyen, T., & Thompson, V. (2009). *QUEST Project: 3D inversion modelling, integration, and visualization of airborne gravity, magnetic, and electromagnetic data, BC, Canada* (Tech. Rep.). Mira Geoscience. Retrieved from http://www.geosciencebc.com/reports/gbcr-2009-15/

Phillips, N., Oldenburg, D., Chen, J., Li, Y., & Routh, P. (2001). Cost effectiveness of geophysical inversions in mineral exploration: Applications at San Nicolas. *The Leading Edge*, *20*(12), 1351–1360. Retrieved from https://doi.org/10.1190/1.1487264 (_eprint: https://doi.org/10.1190/1.1487264) doi: 10.1190/1.1487264

Porter, T., & Duff, T. (1984). Compositing Digital Images. In *Proceedings of the 11th Annual Conference on Computer Graphics and Interactive Techniques* (pp. 253–259). New York, NY, USA: Association for Computing Machinery. Retrieved from https://doi.org/10.1145/800031.808606 doi: 10.1145/800031.808606

Schiarizza, P. (2003). Geology and Mineral Occurrences of Quesnel Terrane, Kliyuk Creek to Johanson Lake (94D/8,9)..

Schiarizza, P. (2014). Geological setting of the Granite Mountain batholith, host to the Gibraltar porphyry Cu-Mo deposit, south-central British Columbia..

Sun, J., Melo, A. T., Kim, J. D., & Wei, X. (2020). Unveiling the 3D undercover structure of a Precambrian intrusive complex by integrating airborne magnetic and gravity gradient data into 3D quasi-geology model building. *Interpretation*, *8*(4), SS15–SS29. Retrieved from https://doi.org/10.1190/INT-2019-0273.1 (_eprint: https://doi.org/10.1190/INT-2019-0273.1) doi: 10.1190/INT-2019-0273.1

Wei, X., & Sun, J. (2021, September). 3D probabilistic geology differentiation using mixed Lp norm joint inversion constrained by petrophysical information. In *First International Meeting for Applied Geoscience & Energy Expanded Abstracts* (pp. 1231–1235). Society of Exploration Geophysicists. Retrieved 2021-09-08, from https://library.seg.org/doi/10.1190/segam2021-3586619.1 doi: 10.1190/segam2021-3586619.1

Williams, N., & Dipple, G. (2007). Mapping Subsurface Alteration Using Gravity and Magnetic Inversion Models. In *Proceedings of the Fifth Decennial International Conference on Mineral Exploration.* (pp. 461–472). Toronto.

Williams, N. C., Lane, R., & Lyons, P. (2004). Towards 3D Maps of Alteration Under Cover: Regional Constrained 3D Inversion of Potential Field Data from the Olympic Cu-Au Province, South Australia. *ASEG Extended Abstracts*, *2004*(1), 1–4. Retrieved from https://doi.org/10.1071/ASEG2004ab160 (Publisher: Taylor & Francis) doi: 10.1071/ASEG2004ab160